Dissertations and Theses

11-2013

Auroral Ion Upflows: Sources, High Altitude Dynamics, and Neutral Wind Effects

Meghan R. Burleigh

Embry-Riddle Aeronautical University - Daytona Beach

Follow this and additional works at: https://commons.erau.edu/edt

Part of the Atmospheric Sciences Commons

AURORAL ION UPFLOWS: SOURCES, HIGH ALTITUDE
DYNAMICS, AND NEUTRAL WIND EFFECTS

BY

MEGHAN R. BURLEIGH

A Thesis

Submitted to the Department of Physical Sciences

and the Committee on Graduate Studies

In partial fulfillment of the requirements

for the degree of

Master in Science in Engineering Physics

12/2013

Embry-Riddle Aeronautical University
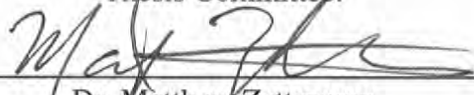
Daytona Beach, Florida

ii

AURORAL ION UPFLOWS: SOURCES, HIGH ALTITUDE
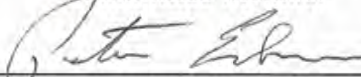DYNAMICS, AND NEUTRAL WIND EFFECTS

by

MEGHAN R. BURLEIGH

This thesis was prepared under the direction of the candidate's Thesis Committee Chair,
Dr. Matthew Zettergren, Assistant Professor, Daytona Beach Campus, and Thesis
Committee Members Dr. John Hughes, Associate Professor, Daytona Beach Campus,
and Dr. Johnathan Snively, Assistant Professor, Daytona Beach Campus, and
has been approved by the Thesis Committee. It was submitted to the
Department of Physical Sciences in partial fulfillment of the
requirements for the degree of
Master of Science in Engineering Physics

Thesis Committee:
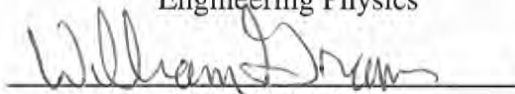
_____
Dr. Matthew Zettergren
Committee Chair
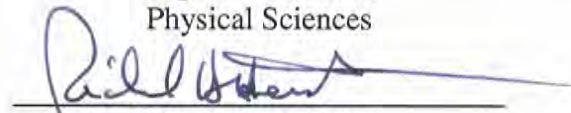
_____
Dr. John Hughes
Committee Member

_____
Dr. Peter Erdman
Graduate Program Chair,
Engineering Physics

_____
Dr. William Grams
Dean, College of Arts and Sciences

_____
Dr. Jonathan Snively
Committee Member

_____
Dr. Terry Oswalt
Department Chair,
Physical Sciences

_____
Dr. Richard Heist
Chief Academic Officer

12/20/2013
Date

Abstract

Large upwellings of thermal plasma are commonly observed in the high-latitude, top-side ionosphere. These auroral ion upflows have a range of potential sources including frictional heating, electron precipitation, neutral winds, and higher-altitude density cavities. The unique signatures and detailed evolution of these upflows are examined through the use of Incoherent Scatter Radar data and a sophisticated ionospheric fluid model.

A survey of solar cycle 23 shows that at Sondrestrom upflows occur most often in the cusp region and midnight auroral zone. Simplified force balance analysis and steady state velocity calculations are applied to a few select events to elucidate the role of the neutral wind in ion upflows. In some cases, the data suggests that neutral winds are necessary to balance the forces at lower altitudes. Detailed modeling shows that neutral winds will directly impact the efficiency of ion upflow mechanisms, and can create factors of $\sim 2-4$ enhancements in upward ion fluxes in the topside ionosphere. Through detailed modeling, it has been shown that the commonly used steady state momentum equations are not consistently valid above ~ 450 km. The significant transient effects, that exist at the high altitudes, imply that instantaneous input/output relationships for parameterizing ion outflow are likely inadequate. Steady state velocity calculations, in both radar data and simulations, tend to grossly over/under

estimate speeds when the ions are accelerating/decelerating at high altitudes.

A systematic simulation study of the efficiency and transient responses of the ionospheric upflow to various energy sources is also conducted. For this study, applied electric potentials were varied from 50 to 150 mV/m in 10 mV/m increments, electron precipitation effects peaking at a range from 2 to 20 mW/m^2 were varied in 2 mW/m^2 increments, and density cavities were varied from 10% depletion up to 80% depletion in 10% increments. These results generally reveal that the propagation time delay between the F-region where the upflows are initiated and higher-altitudes is highly amplitude dependent. Electric fields exceeding 110 mV/m or particle fluxes exceeding 18 mW/m^2 create tremendous fluxes ($\sim10^{13}$ m^{-3} s^{-1}) of plasma that likely act as source populations for other energization processes above the ionosphere. Above 750 km, high altitude responses are not purely wave-like and include the dissipative effects of heat fluxes and heat exchange along with other complexities such as O$^+$ - H resonant charge exchange.

Acknowledgments

I am very grateful to my advisor, Dr. Zettergren, for his expert help and guidance during this work. Without his insights, I would not have been able to accomplish my research goals. I would like to thank my committee members, Dr. Huges and Dr. Snively, for their thoughts and comments. I also would like to thank the entire Physical Science department for always being welcoming no matter whose door I knock on.

Many, many thanks to my fiancé Chand for being so supportive and understanding during this educational experience. Lastly, I would like to thank my mother Celia for always encouraging and believing in me.

Contents

List of Tables

List of Figures

Chapter 1

INTRODUCTION

1.1 Properties and Regions of the Earth's Ionosphere

The Earth's ionosphere is a dynamic portion of the upper atmosphere that is composed of free thermal electrons (< 1 eV) and ions. This region generally ranges in altitude from 60 km to 1000 km and beyond. At high-altitudes (> 100 km), as considered in this study, a wide variety of ion transport, production and loss processes affect the distribution of the ionospheric plasma. Ion production includes photoionization of local neutrals from solar EUV and soft x-ray radiation as well as ionization from collisions of precipitating energetic particles with atmospheric constituents. Once ionized, the plasma will undergo chemical reactions with other ions and neutrals, recombine with electrons, diffuse to higher or lower altitudes, and be transported by neutral winds, electric fields and magnetic fields. A typical daytime ionosphere is presented in Figure 1.1. The ionosphere is often subdivided into four regions: the D, E, F and topside regions.
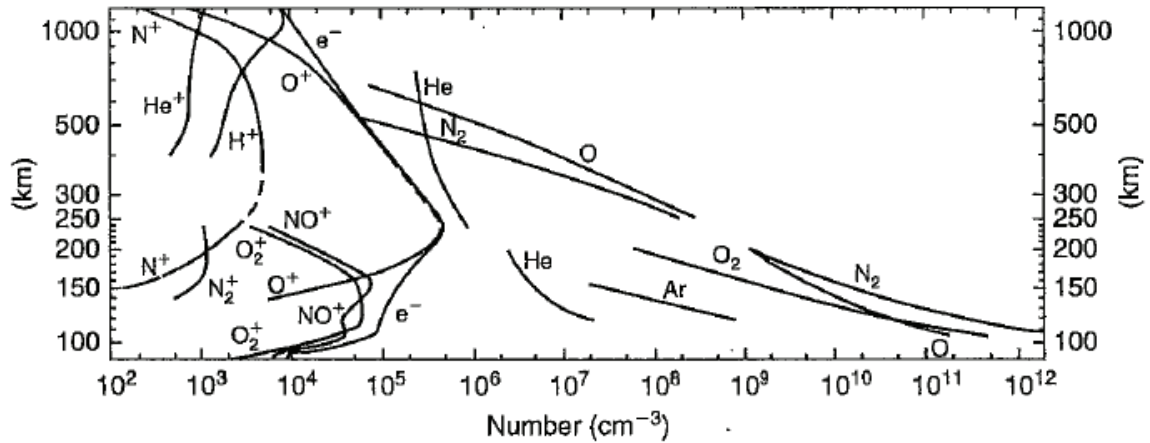
Figure 1.1: Atmospheric densities by species and altitude. Ionospheric peak densities vary by ion species for the D, E, and F-regions. At lower altitudes the neutral population is much much greater than the ion population affecting the chemistry, ionization and recombination rates (Kelley, 2009, p. 6).

The D-region

The D-region extends from ∼60 km up to ∼100 km. Molecular ions dominate this region with NO^+ and O_2^+ being the most abundant (Kelley, 2009, p. 10). The neutral atmosphere is many orders of magnitude denser than the local plasma at these altitudes creating a very high recombination rate and low overall ion density. The D-region becomes indistinct after sunset when the main source of photoionization is gone and recombination takes over.

The E-region

The E-region extends from ∼100 km up to ∼150 km with a peak density of 10^{11} m^{-3} around 110km. The total ion density of this region is less than a millionth of that of the local neutrals (see Figure 1.1). Because of this, the collisions between

ion species do not play a large role in the local plasma dynamics but the collisions between ions and neutrals do. Photoionization and chemical reactions involving N_2 and O_2 create the most abundant ions in this region: N_2^+, NO^+ and O_2^+ (Schunk and Nagy, 2000, p. 30). The main loss process is the recombination of molecular ions with local electrons creating many neural species. The loss of ions is most pronounced just after sunset when the main source of photoionization is gone and recombination reduces the density of the E-region by an order of magnitude or more within minutes of sunset.

The F-region

The F-region, between ∼150 km and ∼1000km, is where more dynamical plasma transport phenomena occur. The peak density is, on average, 10^{12} m^{-3} at ∼300km. Maximum ionization occurs in this region because of a balance between plasma transport processes and chemical loss processes. Photoionization drives the production of the dominant ion species, O^+ (Schunk and Nagy, 2000, p. 31). The main loss process is a 2-step recombination of ions with local neutrals and free electrons yielding O and N. The direct recombination of O^+ with e^- is a secondary loss process but the timescale of this process is much longer than the two step process so the effective loss rate is very small. Ion frictional heating can speed the conversion of O^+ into NO^+ and increase recombination loss rates because the shorter chemical lifetimes of molecular ions (St. Maurice and Laneville, 1998). Overall, there are less molecules than atoms in this region creating longer lifespans of local ions. The recombination rate is slow enough that there is still a perceivable F-region ion density peak at all times, even during the night when the photoionization sources include only weak starlight.

Topside Ionosphere

Above the F-region is the topside ionosphere where the plasma density decreases almost exponentially. At these altitudes above $\sim$1000km the dominant species changes to H^+ from O^+. This is influenced by the neutral atmosphere in which H has replaced O as the dominant species and the fact that the resonant charge exchange process favors the creation of H^+ from O^+ and H (Schunk and Nagy, 2000, p. 96). The overall density of this region is small enough that the few collisions between particles do not play a significant role in the local dynamics and consequently this region is often considered collisionless.

1.2 Plasma Flow

With ion production, loss, and transport occurring within the ionosphere, there are times when large ($>$100 m/s) plasma upflows occur. Several physical situations are known to be able to cause ion upflows. These include heating the ions so that they rise, heating the electrons so that they rise thus creating an ambipolar electric field that accelerates the ions upward, having upflowing local neutral species that result in ions being dragged upward, and/or creating a plasma density gradient that causes upward ion transportation (Remick, 2004).

Many studies have been conducted to characterize the dependent relationships and features of ionospheric upflow. Correlations between the occurrence rates of ion upflows and magnetic local time (MLT) (Keating et al., 1990; Endo et al., 1999), season (Kelley, 2009), solar cycle (Foster et al., 1998; Ogawa et al., 2010), Kp (Foster et al., 1998; Endo et al., 1999; Ogawa et al., 2009) and solar wind (Ogawa et al.,

2009) have been investigated. Efforts have been made to explain the cause of observed field-aligned ion outflows as being due to plasma heating and the resulting plasma expansion (Jones et al., 1988, 1990), expansion of plasma into low density magnetospheric auroral cavities (Singh et al., 1989), field-aligned currents in auroral arcs (Block and Falthammar, 1968), expansion of the neutral atmosphere because of plasma heating (Bates, 1973), and as a response to auroral precipitations (Wahlund et al., 1992; Whitteker, 1977). Despite the many physical processes (and coupling of these processes) that can induce ion upflow, Wahlund et al. (1992) have introduced two categories, type 1 and type 2, which are widely used to classify ion upflows today.

Type 1 ion upflow events are associated with elevated ion temperatures, a strong perpendicular electric field and minimal auroral precipitation. When the ionospheric ions are under the influence of a strong perpendicular (with respect to the magnetic field lines) electric field they move through the local neutral atmosphere and are frictionally heated. This creates anisotropic increases in the ion temperature that result in large pressure gradients that act to push the ions outward (Zettergren and Semeter, 2012). This type of ion upflow can be considered a result from thermal plasma expansion (Foster et al., 1998). Observations of type 1 upflows often also show a lifted F-region peak location, very low electron densities below 300 km and almost no increase in electron temperature (Wahlund et al., 1992).

Type 2 upflow events are associated with elevated electron temperatures and auroral precipitation that increases electron densities at low altitudes (200-300 km). Isotropic ion temperatures and a weak to moderate perpendicular electric field have also been associated with this type of upflow. Found above auroral arcs, which are associated with upward field aligned currents, type 2 upflows seem to occur more

often and are stronger than type 1 upflows (Foster and Lester, 1996; Wahlund et al., 1992; Ogawa et al., 2003).

These two upflow type categories encompass the majority of observed ion upflow events but not all. From statistical studies of topside auroral upflows (Foster et al., 1998; Ogawa et al., 2010), approximately 80% of observed upflow events had an associated increase in electron temperature or F-region density. These are signatures of type 2 upflows. Between 50 to 60% of observed upflows had an increase in ion temperature. This is an indicator of a type 1 upflow. There have also been observed ion upflows with both ion and electron heating present and cases where neither heating signatures are seen (Foster et al., 1998; Ogawa et al., 2009). From the lack of an observed increase in the ion temperature and electron temperature, in conjunction with field aligned velocities greater than 100 m/s, the existence of other upflow mechanisms can be inferred.

Neutral winds, responsible for driving the ions upward, are a likely candidate. Observations by Skjaeveland et al. (2011) found some upflows were greater than expected from ambipolar diffusion alone, suggesting that ion-neutral frictional heating contributed to upflow events in most cases. As discussed in Schunk and Nagy (2000, p. 28) solar forcing, caused by the influence of the EUV and Xrays from the solar wind, is a driver of neutral winds. This effect, driven by a global pressure gradient from day side to night side, will be strongest around solar max. Another potential source of intense neutral winds is provided by magnetosphere-ionosphere coupling in the polar latitudes (Rishbeth and Garriott, 1969). When the ions are moving rapidly in the dual cell convection pattern found in the polar region, motion is imparted to the neutrals from collisions with the ions. Because there are many more neutral particles

than ions, the motion of the ions must be extreme in order for an appreciable amount of momentum to imparted.

Another possible driver of ion upflow is the presence of a high altitude auroral plasma cavity (Benson et al., 1980; Singh et al., 1989). Potentially created by ambipolar electric fields, transverse heating and mirror forces (Ganguli et al., 1988; Singh, 1992), this kind of density cavity would act to draw ions upward much like a vacuum. Using a fluid model of the ionosphere, Calvert (1981) has shown that such a cavity would not only be capable of drawing ions upwards but also in fluxes larger than those from thermal sources.

Certain locations in the ionosphere are more likely to host ion upflows than others. The nighttime polar cap boundary region is one location of energetic upflows which can occur in conjunction with poleward boundary intensifications and high-density plasma patch convection into the upflow channels (Su, 1999; Zettergren et al., 2007; Semeter et al., 2003). Auroral current regions also play an important role in ionospheric upflows. Upward current regions (UCRs) often contain soft electron precipitation resulting in type 2 upflow events. Downward current regions (DCRs) contain intense ion heating resulting in type 1 upflows (see Figure 1.2) even though both recombination loss processes and current closure deplete auroral DCRs (Zettergren and Semeter, 2012). The cusp is another location in which ion upflows are found, and contains both soft precipitation and strong electric fields (Moen et al., 2004).

Once the plasma has undergone heating and expansion resulting in ion upflow, there is the potential for ions to undergo further acceleration through additional mechanisms until escape speeds are reached, resulting in ion outflow to the magnetosphere.
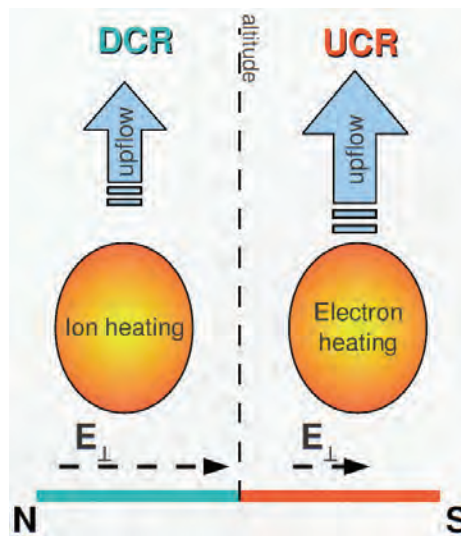
Figure 1.2: Downward current regions often contain large perpendicular electric fields resulting in type 1 upflows. This type of upflow is usually less intense than the type 2 upflows found in the upward current regions that contain middling strength perpendicular electric fields. (Figure by M. Zettergren)

For example, the ions can undergo secondary accelerations perpendicular to the magnetic field from transverse plasma waves (Kintner et al., 1996; Andre et al., 1998). This energizes the plasma perpendicular to the magnetic field and the mirror force then propels the ions to escape velocities. The escape velocity of O^+, the primary ion for much of the F-region and lower topside where ion upflows are occurring, is ~11 km/s. Parallel electric fields associated with auroral acceleration regions (AAR) direct these ion outflows outward to the magnetosphere in the form of ion beams (see Figure 1.3). As a result, the high-latitude ionosphere is the main source of O^+ found in the magnetosphere (Moore and Horwitz, 2007). This multi-step outflow process has been supported by observations of concurrent ion up and outflows (Yoshida et al., 1999; Lynch et al., 2007; Ogawa et al., 2008; Strangeway et al., 2005). The auroral
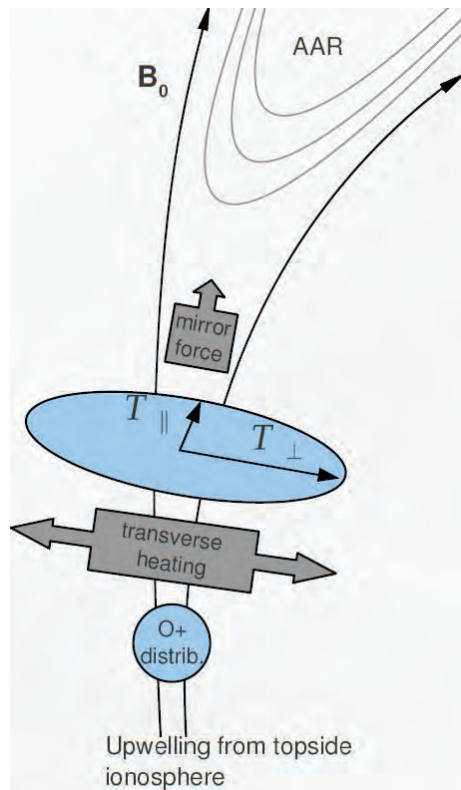
Figure 1.3: Ion upflows from the topside can undergo transverse heating which creates temperature anisotropies. These directional temperature inequalities serve to energize the plasma and the mirror forces then propels the ions up into the auroral acceleration regions. From there the ions are transported outward to the magnetosphere in the form of ion beams. (Figure by M. Zettergren)

zone, and specifically the UCRs and DCRs are sources of many of the ion accelera-tion mechanisms that connect ion upflows to ion outflows, i.e. ionospheric heating, transverse energization and parallel potential structures.

This thesis investigates observations from the Incoherent Scatter Radar at Son-drestrom. The high altitude dynamics of the upflowing populations and their basic characteristics through different physical regimes are examined through synergistic

use of the radar data alongside model results. A statistical overview of the Sondre-strom radar data for solar cycle 23 is presented in Chapter 3. From the analyzed radar data, several data sets are presented in Chapter 4 with a detailed analysis of the features, sources and dynamics of the observed upflowing plasma. Explanations are offered for ion upflow events that do not fall within accepted classifications of up-flow types. Model simulations, in Chapter 5, of the different types of ion drivers give greater insight into the time dependence, nonlinearity and disturbance propagation at different altitudes. Final conclusions of the sources, high altitude dynamics, and neutral wind effects are presented in Chapter 6.

Chapter 2

IONOSPHERIC DYNAMICS

In this thesis, a fluid mathematical model is used to describe ionospheric species. This model is obtained by first considering the velocity distribution of each species and then computing distribution averages. Taking a chunk of some volume d^3r of ionospheric plasma, the ions have a velocity distribution function, $f_s(\vec{r}, \vec{v}_s, t)$ that describes the number of ions for each species that are located within the volume element d^3r and simultaneously have velocities in the velocity space volume element d^3v for any given point in time, t.

The fluid formulation describes the evolution of macroscopically observable quantities including the number density, drift velocity, and thermal energy. The number density, n_s, for each species can be determined by integrating the distribution function with respect to the velocity-space volume element,

$$n_s = \int f_s \, d^3v. \tag{2.1}$$

The drift velocity, $\vec{v}_s$, per species is determined by integrating the product of the

random velocity, $\vec{v}$ and the distribution function with respect to the volume element,

$$\vec{v}_s = \frac{1}{n_s} \int \vec{v} f_s \, d^3 v. \tag{2.2}$$

The thermal energy, written in the form of $\frac{3}{2} k_b T_s$, per species is determined by integrating the product of the kinetic energy and the distribution function with respect to the volume element,

$$\frac{3}{2} k_b T_s = \frac{1}{n_s} \int \frac{m_s (\vec{v} - \vec{v}_s)^2}{2} f_s \, d^3 v, \tag{2.3}$$

where m_s is the species mass, T_s is the species temperature, and k_b is Boltzmann's constant.

The change of the plasma's distribution in space and velocity space can be determined by taking the derivative of $f_s(\vec{r}, \vec{v}_s, t)$. With dt being small and taking into consideration the effect of collisions within the plasma, the limit of the Taylor series expansion of this derivative (Schunk and Nagy, 2000, p. 47) yields the Boltzmann equation,

$$\frac{df_s(\vec{r}, \vec{v}_s, t)}{dt} = \frac{\partial f_s}{\partial t} + \nabla_r \cdot (f_s \vec{v}_s) + \nabla_v \cdot (f_s \vec{a}_s) = \frac{\delta f_s}{\delta t}, \tag{2.4}$$

where t is time, $\vec{v}_s$ is the drift velocity, and $\vec{a}_s$ is the acceleration of species s. Using Equation 2.4, moment equations describing specific aspects of the plasma can be derived. The moments of interest include descriptions for the evolution of the plasma's density, velocity and energy.

Starting with the plasma density, the evolution of an ion species' density is obtained by integrating the Boltzmann equation for all velocities. This produces the general continuity equation,

$$\frac{\partial n_s}{\partial t} + \nabla \cdot (n_s \vec{v}_s) = \frac{\delta n_s}{\delta t}.$$
(2.5)

Each species, s, will have its own continuity equation when describing the plasma as a whole. The evolution of a species' drift velocity is determined by multiplying Boltzmann's equation by the species mass and random velocity and integrating. This yields the momentum equation,

$$n_s m_s \left(\frac{\partial \vec{v}_s}{\partial t} + (\vec{v}_s \cdot \nabla) \vec{v}_s \right) + \nabla \cdot \overleftrightarrow{P}_s - n_s m_s \vec{G} - n_s q_s \left(\vec{E} + \vec{v}_s \times \vec{B} \right) = \frac{\delta M_s}{\delta t},$$
(2.6)

where m_s is the ion mass, $\vec{G}$ is the three dimensional effects of gravity, M_s includes the collisional effects and q_s is the species charge. $\overleftrightarrow{P}_s$ is the pressure tensor described by a higher order moment equation. The evolution of a species' energy is also derived from integrating the product of the Boltzmann equation, $1/2$ the species mass and the random velocity squared. Writing the result in terms of temperature, using the ideal gas law, the energy moment equation is,

$$\frac{\partial T_s}{\partial t} + \nabla \cdot (T_s \vec{v}_s) - \frac{1}{3} T_s (\nabla \cdot \vec{v}_s) + \frac{2}{3 n_s k_b} \nabla \cdot \vec{h}_s = \frac{\delta U_s}{\delta t},$$
(2.7)

where T_s is the temperature for species s and $\vec{h}_s$ is the heat flux. More moment equations, like the heat flow and pressure tensor can be derived to explain the plasma in greater detail but for this study the moments in Equations 2.5, 2.6 and 2.7 are all

that are necessary. Taking these three equations from a general form to an altitudinal and latitudinal specific form is achieved by applying realistic assumptions to the region of interest, as done in Sections 2.1, 2.2, and 2.3. This will allow for collision dominant and collisionless regions, and their respective ion propagation methods, to be described without the need for complicated modeling.

2.1   Force Balanced Momentum Equation

Considering the ionosphere above the radar at Sondrestrom, the near vertical magnetic field lines of this high latitude location makes studying the propagation of plasma along these lines easier. In the lower region of the ionosphere, up to approximately the F-region peak, collisions happen so frequently that a steady state within the plasma is maintained. Working from Equation 2.6, ionospheric pressure in this region is assumed to be isotropic changing the pressure term from a tensor to a scalar. Using the Lorentz gas collision model (Gurnett and Bhattacharjee, 2005) yields,

$$n_s m_s \left(\frac{\partial \vec{v}_s}{\partial t} + (\vec{v}_s \cdot \nabla) \vec{v}_s \right) + \nabla p_s - n_s m_s \vec{G} - n_s q_s \left(\vec{E} + \vec{v}_s \times \vec{B} \right) = n_s \sum_n m_s \nu_{sn} (\vec{v}_n - \vec{v}_s),$$

(2.8)

where ν_{sn} is the collisional frequency between neutral species and the ion species s. The partial pressure is $p_s = n_s k_b T_s$.

Equation 2.8 can be simplified by the momentum equation for electrons. Using the above equation, with electrons as the species, all terms that end up being multiplied by the mass of an electron can be dropped because they are much smaller than everything else of interest, yielding 2.9. This simplified electron momentum equation is used in

the ion momentum equation, Equation 2.8, for $\vec{E}$ to simplify the ion momentum

equation further.

$$\vec{E} = \frac{1}{n_e q_e} \nabla p_e, \tag{2.9}$$

Considering the time independent nature of a steady state system, assuming that

the neutral velocities are zero and selecting only the field aligned components of the

vectors rearranges and simplifies the momentum equation into describing the ions, i,

as,

$$n_i m_i (v_i \cdot \nabla v_i) = - \nabla (n_i k_b T_i) + \frac{n_i q_i}{n_e q_e} \nabla (n_e k_b T_e) + n_i m_i g_{\parallel} - n_i m_i \nu_{in} v_i. \tag{2.10}$$

     Inertia   Pressure Gradients   Gravity   Collisions

This is the Force Balance equation (Wahlund et al., 1992; Skjaeveland et al., 2011).

The effects of inertia, pressure gradients, gravity and collisions balance and the sum of

these Forces per unit area (called forces henceforth) will equal zero during steady state

conditions. If the forces are not balancing then either the system is not appropriately

described by a steady state assumption or a necessary force is not included within

the calculation. In either case, these forces describe the acceleration of the plasma.

2.2 Steady State Velocity and Neutral Winds

Continuing to work within the collisionally dominant region of the ionosphere and neglecting the inertia term reduces Equation 2.10 further:

$$0 = -\nabla(n_i k_b T_i) - \frac{n_i}{n_e} \nabla(n_e k_b T_e) + n_i m_i g_\| - n_i m_i \nu_{in} v_i. \tag{2.11}$$

The two pressure gradients can be combined into a single term $\nabla_\| P$ that encompasses the effects of both the ion pressure gradient and the electron pressure gradient.

$$n_i m_i \nu_{in} v_i = -\nabla_\| P + n_i m_i g_\|. \tag{2.12}$$

Observed velocities, v_o, from radar data include components from both neutral and ion velocities.

$$v_o = v_n + v_{ss}$$

In the desired case of a steady state with no neutral winds the ion velocity, v_i is equal to the steady state velocity, v_{ss}. Thus,

$$v_{ss} = \frac{-\nabla_\| P + n_i m_i g_\|}{n_i m_i \nu_{in}}. \tag{2.13}$$

This equation contains only parameters that are measurable, or inferable, from radar data allowing for v_{ss} to be calculated easily from known local conditions. To determine the presence and magnitude of these neutral winds within collected radar data, a rough estimate can be obtained by subtracting the calculated steady state velocity,

Equation 2.13, from the observed velocity.

$$v_n = v_o - v_{ss}$$
$$= v_o - \frac{-\nabla_\| P + n_i m_i g_\|}{n_i m_i \nu_{in}}$$

This relationship is useful in explaining some of the observed ISR data sets. The amount of wind present at any given point in time is highly variable, though during storm conditions there is a larger probability of high neutral winds. One might speculate that these neutral winds can act to drive ion upflows or add to the velocity of ion upflows created by another source.

2.3   Wave Mode Analysis

Considering the higher altitudes of the ionosphere, from the F-region peak throughout the topside, the plasma transitions from being highly collisional to collisionless. A steady state is unlikely in these altitude regions and disturbances from lower altitudes tend to propagate upward in a wave-like fashion. The number of ion species present in this collisionless region have decreased to the point that the plasma can be described as a two ion plasma or even by a single ion, proton population at high enough altitudes.

2.3.1   Two Ion Plasma

In the topside region, where the ionospheric plasma can be regarded as collisionless, the two dominant species are O^+ and H^+ and is describable locally by six equations: the continuity, momentum and energy equations for H^+ and the continuity, momentum and energy equations for O^+. An ambipolar field, Equation 2.9, was used in

lieu of including the electron momentum equation. At the altitudes in the ionosphere where the two ion plasma is applicable the effects of gravity are small enough to be ignored. Geometric effects of the magnetic field lines are also ignored rendering this a local analysis. Considering the plasma propagation along the field lines, in the "z" direction, these moment equations are in the form:

$$
\begin{aligned}
\text{Continuity}: \quad & \frac{\partial n_s}{\partial t} + \frac{\partial(n_s v_{sz})}{\partial z} = 0 \\[2mm]
\text{Momentum}: \quad & n_s m_s \left(\frac{\partial v_{sz}}{\partial t} + v_{sz} \frac{\partial v_{sz}}{\partial z} \right) + \frac{\partial p_s}{\partial z} - \frac{n_s q_s}{n_e q_e} \frac{\partial p_e}{\partial z} = 0 \\[2mm]
\text{Energy}: \quad & \frac{\partial p_s}{\partial t} + v_{sz} \frac{\partial p_s}{\partial z} + \frac{5}{3} p_s \frac{\partial v_{sz}}{\partial z} = 0.
\end{aligned}
\tag{2.14}
$$

The total electron density, n_e, is equal to the sum of the ion densities, n_H and n_O. By creating a disturbance in the system that is much smaller than background conditions these equations can be linearized. With the disturbance, this allows for the density, velocity and pressure terms to be rewritten as the sum of the background condition ($_0$) and the disturbance ($_1$) for any species ($_s$):

$$
n_s = n_{0s} + n_{1s}
$$

$$
v_{sz} = v_{0s} + v_{1s}
$$

$$
p_s = p_{0s} + p_{1s}
$$

The background parameters are assumed to be temporally and spatially constant thus rendering the partial derivatives with respect to z of these values zero. Also, because the resulting magnitude from multiplying disturbance terms together is much smaller than terms with background conditions, these terms are neglected as well. Thus, the

equations from 2.14 turn into the linearized set of equations below:

$$\text{Continuity}: \quad \frac{\partial n_{1s}}{\partial t} + v_{0s}\frac{\partial n_{1s}}{\partial z} + n_{0s}\frac{\partial v_{1s}}{\partial z} = 0$$

$$\text{Momentum}: \quad \frac{\partial v_{1s}}{\partial t} + \frac{1}{m_s n_{0s}}\frac{\partial p_{1s}}{\partial z} + v_{0s}\frac{\partial v_{1s}}{\partial z} + \frac{k_b T_e}{m_s(n_{0H} + n_{0O})}\frac{\partial n_{1H}}{\partial z}$$

$$+ \frac{k_b T_e}{m_s(n_{0H} + n_{0O})}\frac{\partial n_{1O}}{\partial z} = 0$$

$$\text{Energy}: \quad \frac{\partial p_{1s}}{\partial t} + \frac{5}{3}p_{0s}\frac{\partial v_{1s}}{\partial z} + v_{0s}\frac{\partial p_{1s}}{\partial z} = 0$$

To solve for the wave modes of the two ion plasma, the six linearized equations, three from each ion species, are set into the form

$$\frac{\partial \vec{q}}{\partial t} + \mathbf{A}\frac{\partial \vec{q}}{\partial z} = 0 \qquad\qquad (2.15)$$

where

$$\vec{q} = \begin{bmatrix} n_{1H} \\ n_{1O} \\ v_{1H} \\ v_{1O} \\ p_{1H} \\ p_{1O} \end{bmatrix}$$

and $p_{0s} = n_{0s}k_b T_s$.

Then,

$$\mathbf{A} = \begin{bmatrix} v_{0H} & 0 & n_{0H} & 0 & 0 & 0 \\ 0 & v_{0O} & 0 & n_{0O} & 0 & 0 \\ \dfrac{k_b T_e}{m_H(n_{0H}+n_{0O})} & \dfrac{k_b T_e}{m_H(n_{0H}+n_{0O})} & v_{0H} & 0 & \dfrac{1}{m_H n_{0H}} & 0 \\ \dfrac{k_b T_e}{m_O(n_{0H}+n_{0O})} & \dfrac{k_b T_e}{m_O(n_{0H}+n_{0O})} & 0 & v_{0O} & 0 & \dfrac{1}{m_O n_{0O}} \\ 0 & 0 & \dfrac{5 n_{0H} k_b T_H}{3} & 0 & v_{0H} & 0 \\ 0 & 0 & 0 & \dfrac{5 n_{0O} k_b T_O}{3} & 0 & v_{0O} \end{bmatrix}.$$

The constant matrix $\mathbf{A}$ yields the propagation speeds for each ion when solved for it's eigenvalues. Fourier transforming Equation 2.15, using the transform convention

$$q = \frac{1}{(2\pi)^4} \int_{-\infty}^{\infty} \int_{-\infty}^{\infty} \tilde{q} e^{(ikz - i\omega t)} dk \, d\omega, \tag{2.16}$$

gives

$$-i\omega \tilde{q} + \mathbf{A} i k \tilde{q} = 0. \tag{2.17}$$

This can be simplified and rearranged into

$$\left(\frac{\omega}{k} \mathbf{I} - \mathbf{A} \right) \tilde{q} = 0 \tag{2.18}$$

where $\mathbf{I}$ is the identity matrix and ω/k is equal to the wave phase speeds. Equation 2.18 has a nontrivial solution only if the matrix $\mathbf{A}$ is singular (determinant is equal to zero). This creates an eigenvalue problem where the wave phase speeds are given

by the eigenvalues of $\mathbf{A}$. These eigenvalues, when there is no background drift, are

$$\lambda = \begin{cases} 0 \\ \pm v_{phH} \\ \pm v_{phO} \end{cases}$$

where v_{phH} and v_{phO} are the propagation speeds for H^+ and O^+ respectively. The terms within the propagation speeds are very long and not reproduced in detail here. These wave phase speeds are dependent on the number density of each ion with respect to the bulk plasma. The higher the percentage the plasma is of a particular ion the faster that ion's wave speed is. The upper bound of this is the propagation speed, when the ion is at 100% of the whole. This is the equivalent of a single ion plasma as calculated in the following Section. The lower bound, as ion density ratios become small (and with no background drift), simplifies to

$$v_{phs} = \sqrt{\frac{5k_b T_s}{3m}}$$

for species s, which is the lower dashed lines on Figure 2.1. This indicates that the minor species propagate independent of the electrons when their density is low enough.

Filling in matrix A with realistic example values, $T_H = 3000K$, $T_O = 3000K$, and $T_e = 4000K$, yields the velocities plotted in Figure 2.1 when the background drift velocity, v_{0s}, is equal to zero. When the background drift velocity is not equal to zero, the propagation speeds are simply added to the background velocity. The eigenvalues of matrix $\mathbf{A}$ support this. The solid red line in Figure 2.1 corresponds to
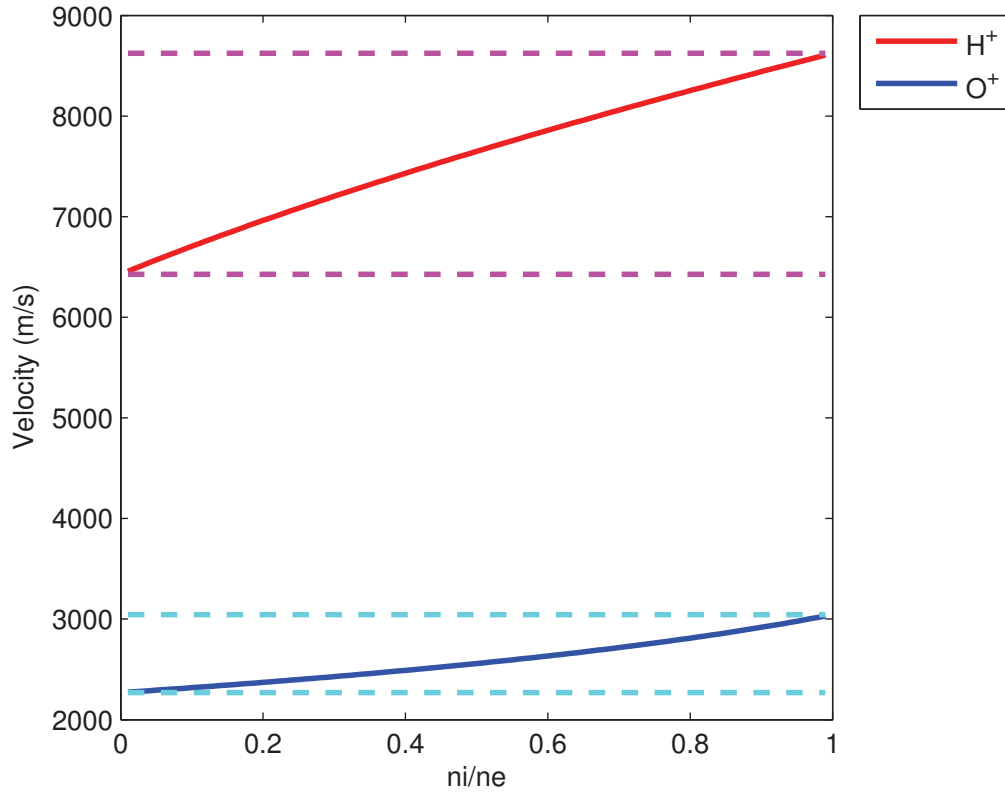
Figure 2.1: Calculated for the example situation presented in Section 2.3.1 without any background drift velocities the phase speeds for an ion species is a function of the ion density ratio. The upper bounding pink or blue dashed line is the velocity achieved if the system was only a single ion. The lower bounding dashed pink or blue line corresponds to the calculated speed if there were no electric field effects.

the H^+ values and the solid blue line corresponds to the O^+ values. For example, when the plasma is a mix, 50% H^+ and 50% O^+, the wave speeds are 7649.0 m/s and 2558.4 m/s respectively. When the plasma is 25% H^+ and 75% O^+ the speeds are 7084.4 m/s and 2762.3 m/s respectively. There is not a dependence between the wave speeds and the total density of the system. The dependance is to the ratios of the ion densities.

2.3.2 One Ion Plasma

At even higher altitudes, greater than 1000km, the ionospheric plasma is collisionless and completely dominated by H^+. This single ion plasma is locally describable by only three equations: the continuity, momentum and energy equations for H^+. Considering the propagation along the "z" direction, the moment equations used to describe the plasma are in the form:

$$\text{Continuity}: \quad \frac{\partial n_s}{\partial t} + \frac{\partial (n_s v_{sz})}{\partial z} = 0$$

$$\text{Momentum}: \quad n_s m_s \left(\frac{\partial v_{sz}}{\partial t} + v_{sz} \frac{\partial v_{sz}}{\partial z} \right) + \frac{\partial p_s}{\partial z} - \frac{n_s q_s}{n_e q_e} \frac{\partial p_e}{\partial z} = 0$$

$$\text{Energy}: \quad \frac{\partial p_s}{\partial t} + v_{sz} \frac{\partial p_s}{\partial z} + \frac{5}{3} p_s \frac{\partial v_{sz}}{\partial z} = 0.$$

Because there is only a single ion under consideration the ion density is equal to the electron density. At this point the species subscript is dropped for ease of notation. Applying the same assumptions and conditions used to linearize the two ion plasma, the three equations for the single ion plasma become:

$$\text{Continuity}: \quad \frac{\partial n_1}{\partial t} + v_0 \frac{\partial n_1}{\partial z} + n_0 \frac{\partial v_1}{\partial z} = 0$$

$$\text{Momentum}: \quad \frac{\partial v_1}{\partial t} + \frac{1}{mn_0} \frac{\partial p_1}{\partial z} + v_0 \frac{\partial v_1}{\partial z} + \frac{k_b T_e}{mn_0} \frac{\partial n_1}{\partial z} = 0$$

$$\text{Energy}: \quad \frac{\partial p_1}{\partial t} + \frac{5}{3} p_0 \frac{\partial v_1}{\partial z} + v_0 \frac{\partial p_1}{\partial z} = 0$$

These linearized equations yield a much simpler version of Equation 2.15 where

now for the one ion plasma:

$$\vec{q} = \begin{bmatrix} n_{1H} \\ v_{1H} \\ p_{1H} \end{bmatrix}$$

and with $p_0 = n_0 k_b T_H$ then,

$$\mathbf{A} = \begin{bmatrix} v_0 & n_0 & 0 \\ \frac{k_b T_e}{m n_0} & v_0 & \frac{1}{m n_0} \\ 0 & \frac{5 n_0 k_b T_H}{3} & v_0 \end{bmatrix}.$$

The eigenvalues, λ, of $\mathbf{A}$ are much simpler and are not dependent on density ratios.

$$\lambda = \begin{cases} v_0 \\ v_0 \pm \sqrt{\dfrac{k_b T_e}{m} + \dfrac{5 k_b T_H}{3m}} \end{cases}$$

The single ion plasma supports small perturbations propagating at either the background drift speed or at some velocity with or against the background flow. The latter two modes are sound waves influenced by the ambipolar field. By applying the same physical system as used as an example with the two ion plasma, the upper dashed lines of Figure 2.1 are created from the wave speed of H^+ which is 8623.9 m/s when the background drift velocity is set to zero.

Some ionospheric complexities are not captured by these simplified calculations. For example the collisional drag effects of waves is not taken into consideration as well as dispersion from differing thermal conductivities. Both of these would act to modify the disturbance propagation speeds as the local conditions would change. To capture these effects more complex calculations are needed.

Chapter 3

RADAR DATA SURVEY

3.1 Sondrestrom Incoherent Scatter Radar

The Sondrestrom Upper Atmospheric Research Facility is a prime location to observe and study the behavior of plasma in the ionosphere. Located in Kangerlussuaq, Greenland near the Arctic Circle at 66.985601 N, 309.054054 E, this ground station often sits directly under the Auroral Oval. The facility is operated by SRI International in Menlo Park, CA and consists of more than twenty instruments that measure many of the features of the arctic atmosphere. The instrument at Sondrestrom that is important for this study is the L-band (1290MHz) incoherent scatter radar (ISR).

This ISR is a 32 m fully steerable antenna that is used to measure the electron-number density by the total scattered power, the ion temperature to ion mass ratio from the spectral width, the electron temperature to ion temperature ratio from the signal peak to valley ratio, and line of sight ion velocity along the radar beam from the signal's doppler shift. A more thorough discussion of ISR theory can be found in Sheffield et al. (2011). Using an ion composition profile, specific values for ion

temperature and electron temperature can be determined (Zettergren et al., 2011). With the radar antenna being fully steerable these measurements can be determined as functions of azmuth, elevation and range. Data from radar beam positions aligned with the local magnetic field lines only have been selected for this study. When not in alignment with the local magnetic field lines, it is difficult to accurately determine the parallel and perpendicular components of the observed velocity.

3.2   Event Selection Process

Focusing on the date range encompassed by solar cycle 23, (1998-2006), times of ion upflow are searched for in the Madrigal database of Sondrestrom's ISR observations. Looking for periods of time with an observed upward flowing velocity greater than 100 m/s, within the 963 recorded observation times from solar cycle 23, 98 data files were retained from this first search containing the desired ion upflow conditions. It should be noted that some files, especially the files of extended periods of time, contained multiple upflow events. Only the cases in which the radar beam was aligned with the local magnetic field lines are retained. Eliminating non-aligned data sets leaves 35 data files containing 61 observed upflow events.

Table 3.1: Process of Elimination for Upflow Event Datasets

Condition	Data Files
Incoherent Scatter Radar Observations 1998-2006	963
Observed Upward Velocity > 100 m/s	98
Field Aligned Radar Beam During Observations	35
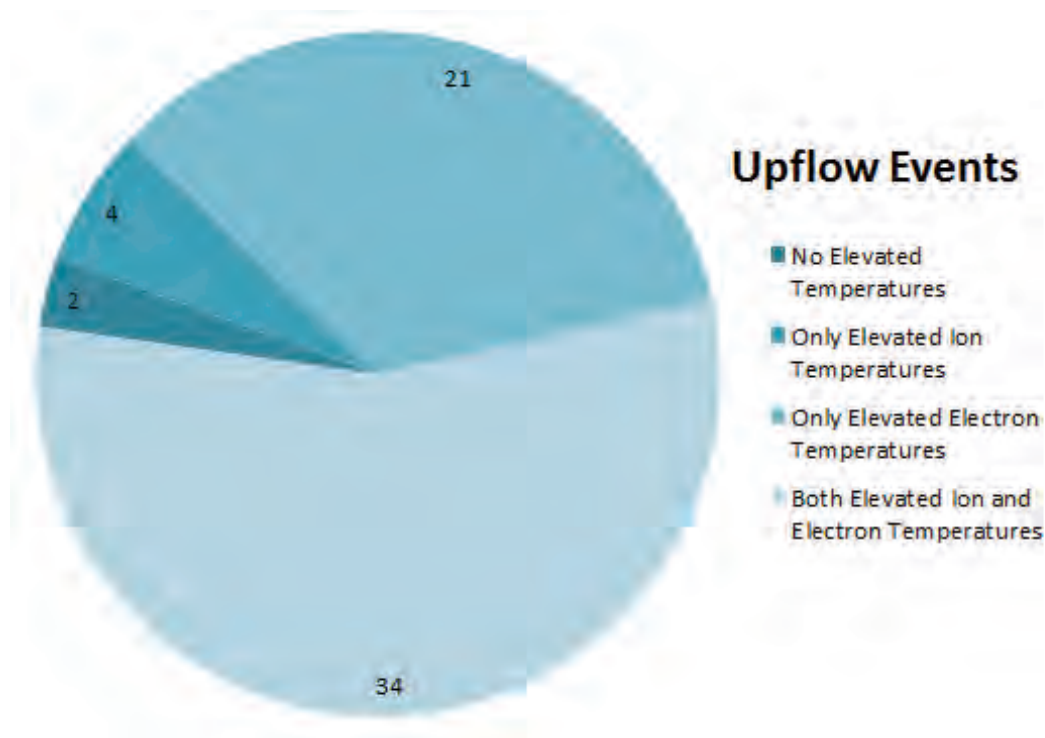
Figure 3.1: The frequency of occurance of selected ISR upflow events as a function of elevated temperatures.

Of these upflows, from the background conditions the majority had elevated electron temperatures and/or elevated ion temperatures. This is where the ion temperatures are raised above 2000K and electron temperatures are raised above 3000K. A few upflow events lacked the expected elevated temperature signatures in conjunction with an increase in electron density and/or a lifted F-region peak thus failing to fall within the type 1 or type 2 categorizes. Of the 61 observed upflow events with line-of-sight velocities greater than 100 m/s, 34 had both elevated ion and electron temperatures, 21 had only elevated electron temperatures, 4 had only elevated ion temperatures, and 2 did not have elevated temperatures (see Figure 3.1). The time of

day of upflow occurrence also varies from event to event with general trends emerging
when plotted in Figure 3.2. A brief summary of the 61 upflows is presented in Table
3.2 including the original file name and experiment being conducted as well as the
date, time, temperature signatures present for each upflow.

Table 3.2: Selected data files containing upflow events. Note: In the columns Ion Temp.
and Electron Temp., 1 indicates elevated above background conditions and 0 indicates not
elevated above background conditions.

File Name	Event Date	Ion Temp.	Electron Temp.	Time (UT)	Original Experiment Type
980228g003	2/28/1998	1	1	23:40	Auroral Emissions Optics
991204g001	12/4/1999	1	1	16:00	Data Acquisition System
991207g001	12/7/1999	0	1	22:50	Auroral Emissions Optics
991207g001	12/8/1999	1	1	00:25	Auroral Emissions Optics
991210g001	12/10/1999	0	0	01:40	World Day (POLITE)
000201g001	2/2/2000	0	0	00:20	Auroral Emissions Optics
000201g001	2/2/2000	0	1	01:05	Auroral Emissions Optics
000213g001	2/13/2000	1	0	05:20	Auroral Emissions Optics
000308g011	3/8/2000	1	1	02:05	
011106g017	11/6/2001	1	1	02:45	CME Monitoring
020123g003	1/23/2002	0	1	17:30	With Oersted and ISTP Sats
020205g007	2/5/2002	1	1	16:50	With TIMED and ISTP Sats
020205g011	2/6/2002	1	1	00:30	With TIMED and ISTP Sats
020211g003	2/11/2002	1	1	23:10	With TIMED and ISTP Sats
020211g003	2/12/2002	0	0	03:15	With TIMED and ISTP Sats
020211g003	2/12/2002	0	1	02:00	With TIMED and ISTP Sats
020211g003	2/12/2002	1	1	00:00	With TIMED and ISTP Sats
020211g003	2/12/2002	1	1	02:40	With TIMED and ISTP Sats
020306g003	3/6/2002	1	1	13:45	With ISTP Sats
020306g003	3/6/2002	1	1	14:30	With ISTP Sats
020907g003	9/7/2002	1	1	14:30	
020907g003	9/7/2002	1	1	16:15	
021028g003	10/28/2002	0	1	23:15	
030108g003	1/8/2003	0	1	22:50	
030214g003	2/14/2003	1	1	11:45	With ISTP Sats
030214g003	2/14/2003	1	1	13:50	With ISTP Sats

File Name Cont...	Event Date	Ion Temp.	Electron Temp.	Time (UT)	Original Experiment Type
030214g003	2/14/2003	1	1	15:30	With ISTP Sats
030214g003	2/14/2003	1	1	17:00	With ISTP Sats
030308g007	3/8/2003	0	1	02:05	F-region winds with FPI
030308g007	3/8/2003	1	0	00:50	F-region winds with FPI
030308g007	3/8/2003	1	0	03:30	F-region winds with FPI
030310g007	3/10/2003	1	1	01:00	F-region winds with FPI
030310g007	3/10/2003	1	1	04:30	F-region winds with FPI
030311g007	3/11/2003	0	1	01:00	F-region winds with FPI
030311g007	3/11/2003	0	1	02:00	F-region winds with FPI
030531g003	5/31/2003	0	1	02:30	Solar Eclipse, CME monitor
030531g003	5/31/2003	0	1	06:15	Solar Eclipse, CME monitor
030624g003	6/25/2003	0	1	23:30	World Days
030624g003	6/26/2003	1	1	09:15	World Days
031029g003	10/29/2003	1	1	11:50	CME Event Monitoring
031029g003	10/29/2003	1	1	15:00	CME Event Monitoring
031029g003	10/29/2003	1	1	23:50	CME Event Monitoring
031029g003	10/30/2003	0	1	12:00	CME Event Monitoring
031029g003	10/30/2003	1	1	23:00	CME Event Monitoring
040122g007	1/22/2004	1	1	14:50	CME Event Monitoring
040722g003	7/22/2004	0	1	14:30	Cluster, TIMED, ISTP Sats
040726g003	7/26/2004	1	1	02:10	CME Event Monitoring
041206g003	12/6/2004	0	1	12:50	World Days
050206g009	2/6/2005	0	1	23:30	Cluster, TIMED, ISTP Sats
050206g009	2/7/2005	0	1	01:15	Cluster, TIMED, ISTP Sats
050206g009	2/7/2005	0	1	03:50	Cluster, TIMED, ISTP Sats
050214g007	2/15/2005	0	1	00:00	With DMSP and ISTP Sats
050214g007	2/15/2005	1	1	03:20	With DMSP and ISTP Sats
050220g007	2/21/2005	1	1	02:40	With TIMED and ISTP Sats
050316g003	3/16/2005	1	0	23:40	With ISTP Sats
050404g003	4/4/2005	1	1	21:15	With ISTP Sats
050404g003	4/4/2005	1	1	22:00	With ISTP Sats
050404g003	4/4/2005	1	1	23:40	With ISTP Sats
060223g003	2/22/2006	0	0	23:45	With ISTP Sats
060530g003	5/30/2006	1	1	03:50	With ISTP Sats
061220g003	12/20/2006	0	1	22:55	Auroral Emissions Optics
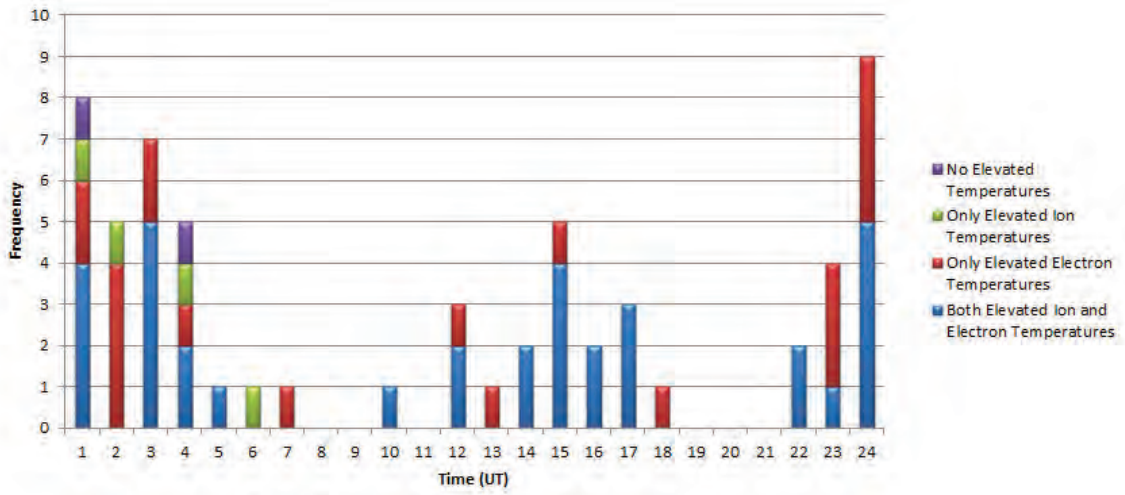
Figure 3.2: Times that the different types of temperature signatures were occurring for the selected ISR data upflow files.

Sorting these observations by the time that the upflow occurred, in universal time (UT), creates a double peaked histogram, Figure 3.2. The two peak upflow occurrence times are around noon and shortly before midnight local time (LT). The
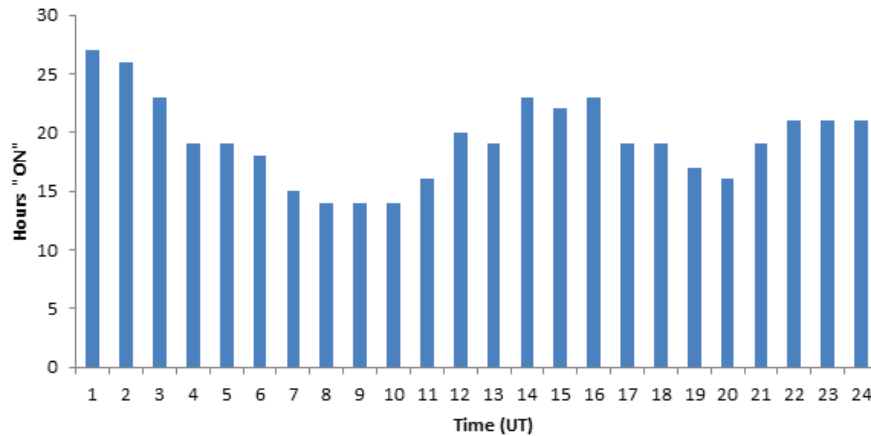
Figure 3.3: The amount of time for each hour of the day that Sondrestrom's ISR was on and collecting data during solar cycle 23.

total amount of time that Sondrestrom's ISR was collecting data, for all of the files listed in Table 3.2, seperated by hour of the day is shown in Figure 3.3. Universal time at Sondrestrom is three hours ahead of local time. This means that noon LT is 15 UT and midnight is 3 UT. By dividing the frequency of upflow events, binned by the time of day, by the amount of hours that the Sondrestrom ISR was collecting data, per hour bin, will determine if any bias has been introduced by the fact that the ISR is on more often at noon and midnight.
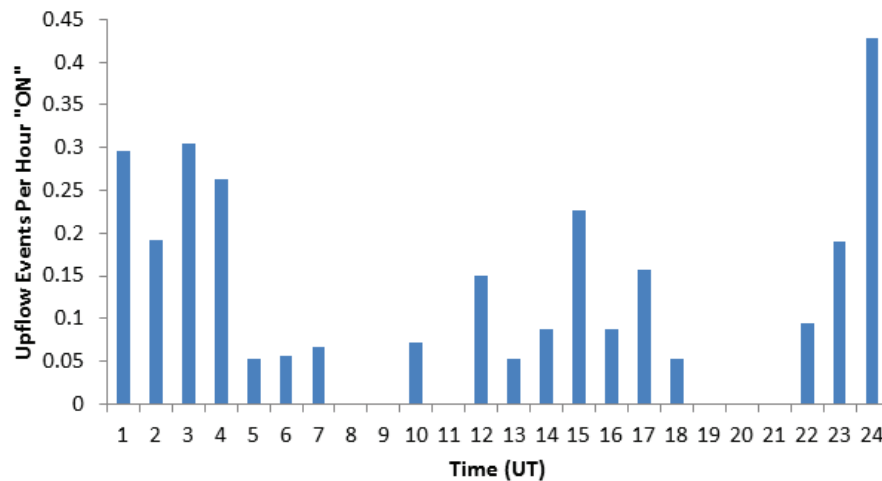
Figure 3.4: Observed upflow events per on hour of the ISR "ON" time as a function of the time of day for the years 1998-2006.

While the amount of time that the radar is on tends to be concentrated around anticipated interesting times, there is not a significant bias introduced by this trend. Figure 3.4 mirrors closely the original double peak occurrence rate see in Figure 3.2. The double peak in the occurrence rate is ultimately caused by natural, physical phenomena, and the histogram illustrates the times when ion upflow are most likely to

occur. The peak around noon and midnight are associated with the cusp and midnight auroral zones respectively and these are the regions where the magnetosphere is adding a lot of energy into the ionosphere increasing the occurrence rates of ion upflows (Moore and Horwitz, 2007). These statistical survey results are consistent with other surveys at other stations (Keating et al., 1990; Foster et al., 1998; Endo et al., 1999; Remick, 2004).

Chapter 4

DETAILED ISR OBSERVATIONS

4.1 Observations of Type 1 and Type 2 Upflows

Type 1 and type 2 ion upflows can be identified by their unique radar signatures and relationships. As discussed in Section 1.2, type 1 upflows are associated with elevated ion temperatures, a strong perpendicular electric field and minimal auroral precipitation. Type 2 upflows are associated with elevated electron temperatures and auroral precipitation that increases electron densities at low altitudes (90-250 km). ISR data contains information about the electron density, ion temperature, electron temperature and the line of sight velocity along the radar beam. Examining these four pieces of information can identify what type of upflow is occurring as well as how the plasma is reacting to the influence of different energy sources. All of the data presented in the following Sections are from solar cycle 23 during periods of time when the radar beam is aligned with the local magnetic field lines to avoid the difficulty of accurately determining the parallel and perpendicular components of an observed velocity.

4.1.1 Type 1 Upflow

The observation on 02/13/2000 at Sondrestrom contains a clear example of a type 1 upflow event and is presented in Figure 4.1. The four panels of radar data include, in descending order: electron density, ion temperature, electron temperature, and
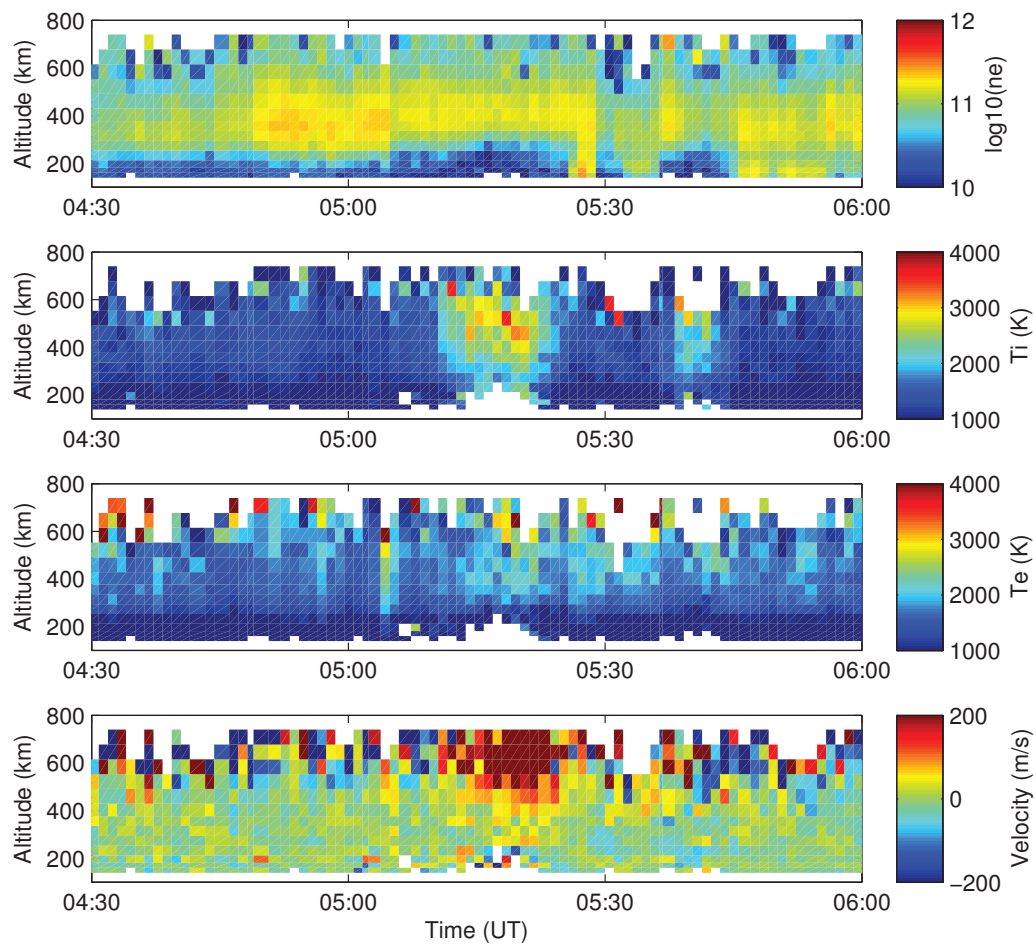
Figure 4.1: A type 1 upflow event seen in the radar data from 02/13/2000. The large upward velocities (panel 4) around 05:20 UT correspond to the elevated ion temperatures (panel 2) identifying this as a type 1 upflow event.

line-of-sight velocity along the radar beam. From 5:15 UT to 5:25 UT there is a very strong upward ion velocity exceeding 200 m/s at altitudes greater than 500 km. Even in the region from 300 km - 450 km there are upflowing ions at speeds greater than 100 m/s (panel 4). During this same span of time the ion temperature increases to around 3000 K (panel 2). The F-region peak is well defined and slightly lifted during the course of this event. There is not a corresonding increase in electron temperature (panel 3) or in the E-region density indicating the lack of electron precipitation (panel 1) during this time of type 1 upflow.

Using Equation 2.10 the primary forces (Forces per unit volume) assumed to be acting within the ionosphere are calculated. These are described by the equations in Table 4.1 include the pressure gradient, effects of gravity, inertia, and collisions. The motion, upward or downward, of the ions are a response to these forces and in steady state conditions the forces should balance out to zero.

Table 4.1: Equations used in the force balance analysis.

Acting Forces	Describing Equation
Pressure (Gradient)	$-\nabla P_{\parallel}$
Gravity	$n_i m_i g_{\parallel}$
Inertia	$-n_i m_i (v_i \cdot \nabla v_i)$
Collisions	$-n_i m_i \nu_{in} v_i$

These four components are shown in Figure 4.2 for the observed upflow on 02/13/2000 at Sondrestrom. The pressure gradient (panel 1) is positive in the regions above the F-region peak and negative in the regions below. With the large amount of ions at the F-region peak there is an "outward" pressure. Gravity (panel 2) is always downward and is proportional to the local density at any altitude. The calculated inertia (panel 3) is several orders of magnitude smaller than the other forces. The collisional forces
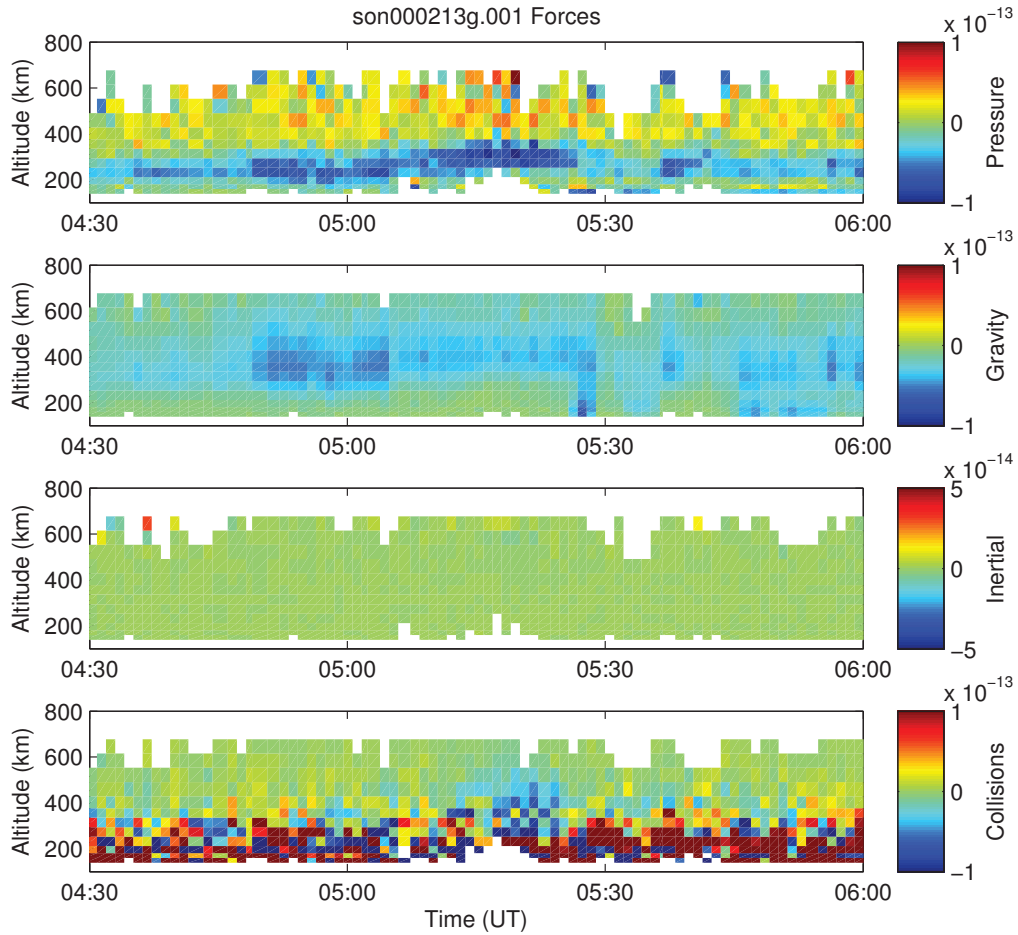
Figure 4.2: The calculated forces from the observations taken on 02/13/2000 at Sondrestrom. From 5:15 UT to 5:25 UT there is a type 1 upflow occurring.

(panel 4) are either positive or negative corresponding to the upward or downward motion of the ions respectively. The sum of these forces, shown in Figure 4.3, are related to the acceleration of the ions. This sum is not balanced as the steady state assumptions indicate it should be; there are periods of strong upward and downward acting forces throughout the lower altitudes (<400 km) where collisions dominate.

For altitudes >400 km, the imbalance is less extreme. The imbalance suggests the influence of other forces not included in the force balance equation, like neutral winds or a non steady state plasma acceleration, but the exact cause is indeterminate.
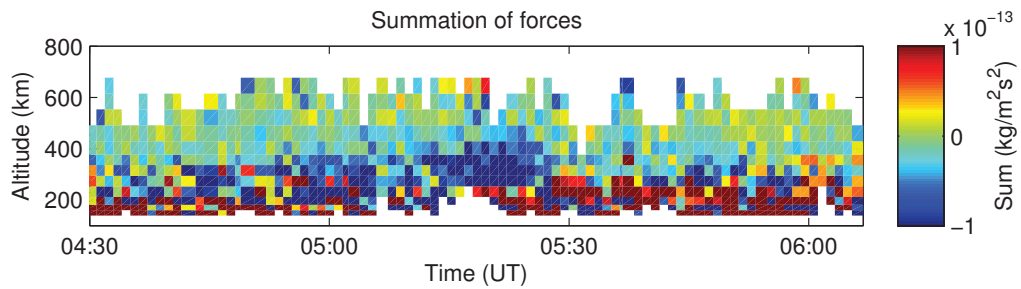
Figure 4.3: The summation of the calculated forces, from the observations taken on 02/13/2000 at Sondrestrom, is dominated by the collisional forces. From 5:15 UT to 5:25 UT there is a type 1 upflow.
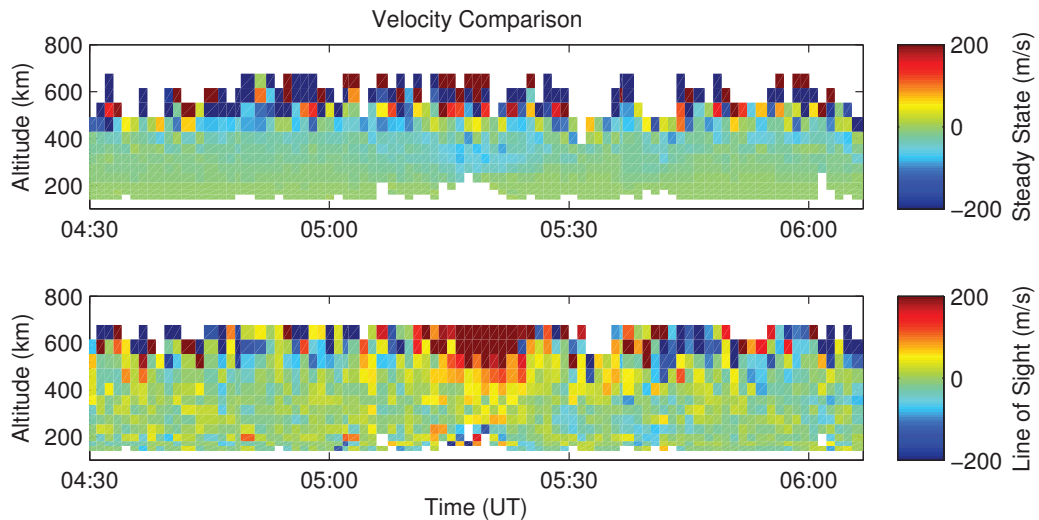
Figure 4.4: The calculated steady state velocity (panel 1) and the observed velocity (panel 2) from 02/13/2000 at Sondrestrom. The calculated steady state velocity does not accurately reproduce the observed upflow.

Using Equation 2.13, the steady state velocity can be calculated and compared to the observed line-of-sight velocity from the radar in Figure 4.4. The steady state velocity (panel 1), for altitudes lower than 450 km, is loosely consistent with the observed velocities when there are no strong upflows. During the main upflow event, when large positive velocities are observed, the steady state velocity calculation predicts downflow. For altitudes greater than 450 km the steady state velocity tends to over or under estimated the velocity by a very large degree.

4.1.2 Type 2 Upflow

The observation on 02/28/1998 at Sondrestrom contains a clear example of a type 2 upflow event, Figure 4.5. The four panels of radar data include the electron density, ion temperature, electron temperature and line of sight velocity along the radar beam. Starting at 23:35 UT, an increase in the E-region electron density is observed (panel 1). This increase occurs several times over the next 25 minutes suggesting the presence of intermittent precipitating electrons. A clear ion upflow is occurring during this time with velocities exceeding 200 m/s at altitudes greater than 450 km; even at 300 km velocities are greater than 75 m/s (panel 4). There is a corresponding increase in electron temperature from 1000 K to over 4000 K (panel 3) during this time as well. The slight increase in ion temperature is likely caused by collisional heat transfer and possibly not directly caused by the precipitating electrons (panel 2).

Applying the force balance equation to the ISR data yields the forces presented in Figure 4.6. The pressure gradient (panel 1) has a positive gradient above the F-region peak and a negative gradient below as the high density there acts to push the ions outward from the peak. When there is an increase in the low altitude electron density
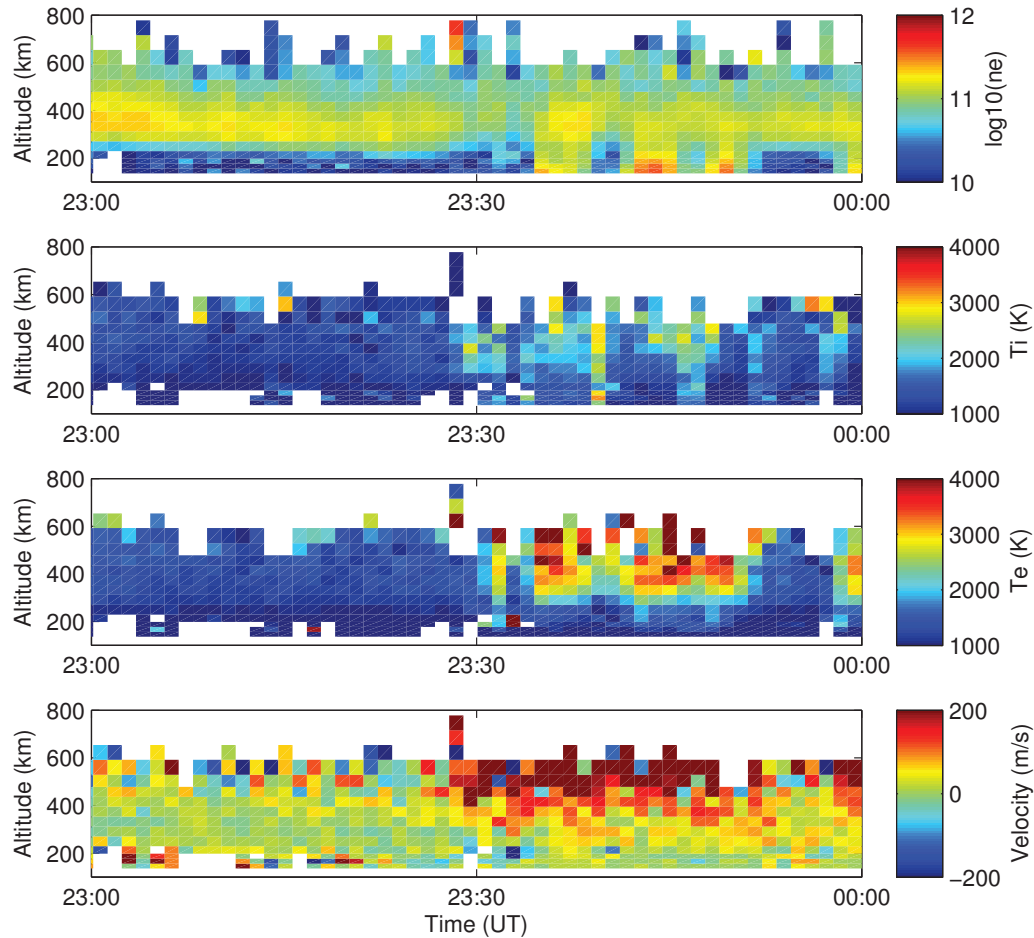
Figure 4.5: A clear observed Type 2 upflow radar data on 02/28/1998. The large upward velocities (panel 4) around 23:35 UT correspond to the elevated electron temperatures (panel 3) and the low altitude, electron density increases (panel 1).

there is a corresponding positive pressure gradient in this area from that increase as well as an increase in the calculated effects of gravity (panel 2). The inertia (panel 3) is several orders of magnitude smaller that the other calculated values and doesn't play a large role in determining the dynamics of the situation. The collisions within
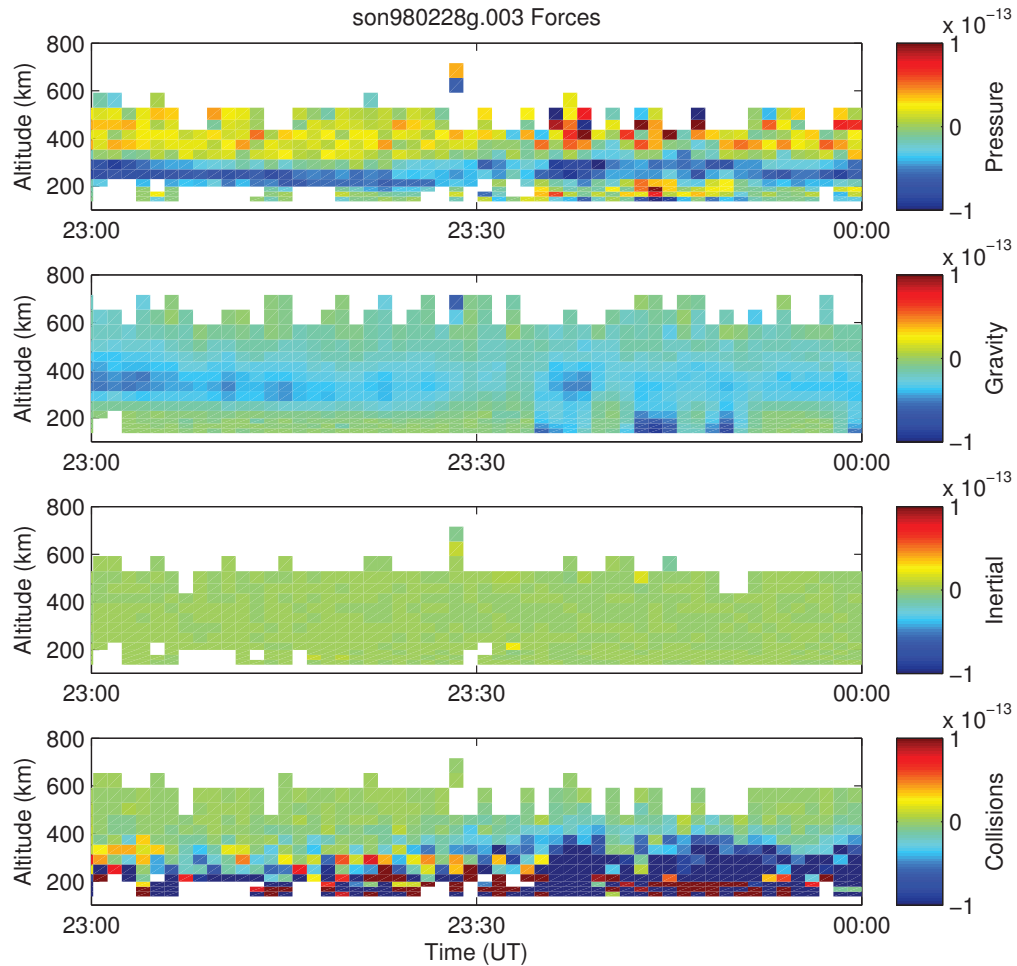
Figure 4.6: Force balance analysis of the Type 2 upflow radar data on 02/28/1998. The positive pressure gradient (panel 1) in the E-region, centered around 23:45 UT, correspond to the increased gravitational effects (panel 2). Inertia (panel 3) is much much smaller than the other forces and does not dictate the acceleration to an appreciable degree. The collisions (panel 4) act against the direction of ion flow creating the large downward forces during the times of ion upflow.

the ionosphere are proportional to the observed velocity and the rate of collisions has

been determined by MSIS (panel 4). The sum of the four panels in Figure 4.6 produce

Figure 4.7. During the type 2 ion upflow, centered around 23:45 UT, the sum of the forces is negative and dominated by the collisional component of the force balance analysis.
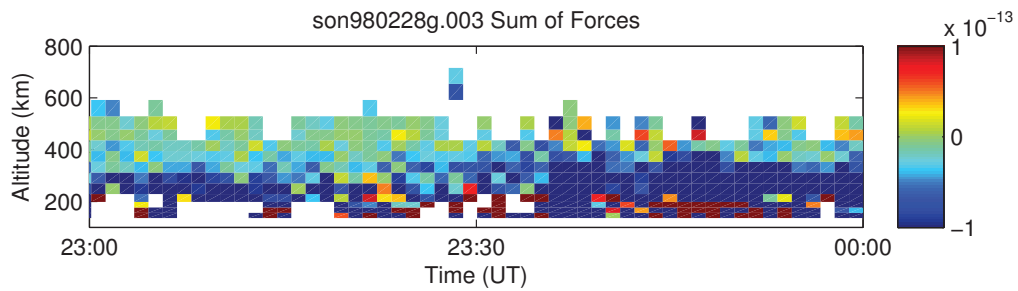
Figure 4.7: Resulting from the force balance analysis of the Type 2 upflow radar data on 02/28/1998, this is the sum of the four terms in Figure 4.6. At lower altitudes the collisional forces dominate the summation creating large negative regions of this plot.
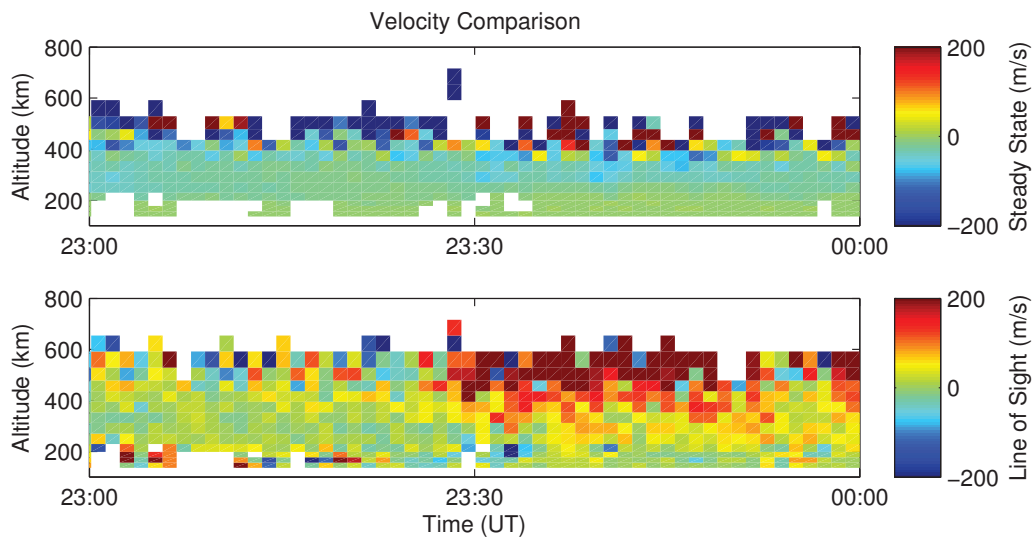
Figure 4.8: The top panel is the calculated steady state velocity for the Type 2 ion upflow on 02/28/1998. The bottom panel is the observed velocity for comparison. During the upflow event the two velocities do not match.

The steady state velocity, calculated using Equation 2.13, gives the top panel of Figure 4.8. The observed line of sight radar velocity (panel 2) does not match well with the calculated steady state velocity especially during the upflow event. During the ion upflow time, for this type 2 upflow, the calculated steady state velocity is small and generally negative for lower altitudes (<450 km) or large and negative, on average, for higher altitudes (>450 km).

4.1.3 Additional Type 1 & 2 Upflows

The observations from 12/07/1999 to 12/08/1999 at Sondrestrom, presented in Figure 4.9, contain multiple upflows of both type 1 and type 2. At 22:45 UT a type 2 upflow begins. The observed velocity reaches over 200 m/s at altitudes greater than 450 km. Even at 300 km the velocity is greater than 75 m/s (panel 4). There is an increase in the E-region electron densities by several orders of magnitude (panel 1) and an increase in the electron temperature to 2000-3000 K (panel 3). The ion temperature is unaffected (panel 2) during this same period of time. From 0:05 UT to 0:25 UT there is another type 2 upflow event. The electron densities increase substantially in the E-region (panel 1). There is an increase in the electron temperature to 2000-2500 K (panel 3) and at higher altitudes, above 500 km, the upflowing ions reach speeds greater than 200 m/s. Even as low as 300 km the velocity is greater than 100 m/s (panel 4). The ion temperature (panel 2) for this time period is unaffected. At 0:25 UT there is a type 1 ion upflow observed for just a few minutes until it either ended or moved out of the radar beam. The ion temperature increases to 3000-4000 K (panel 2). This increase appears to be large enough to explain the increase in electron temperature to 2000-3000 K through heat exchange from the ions (panel 3).
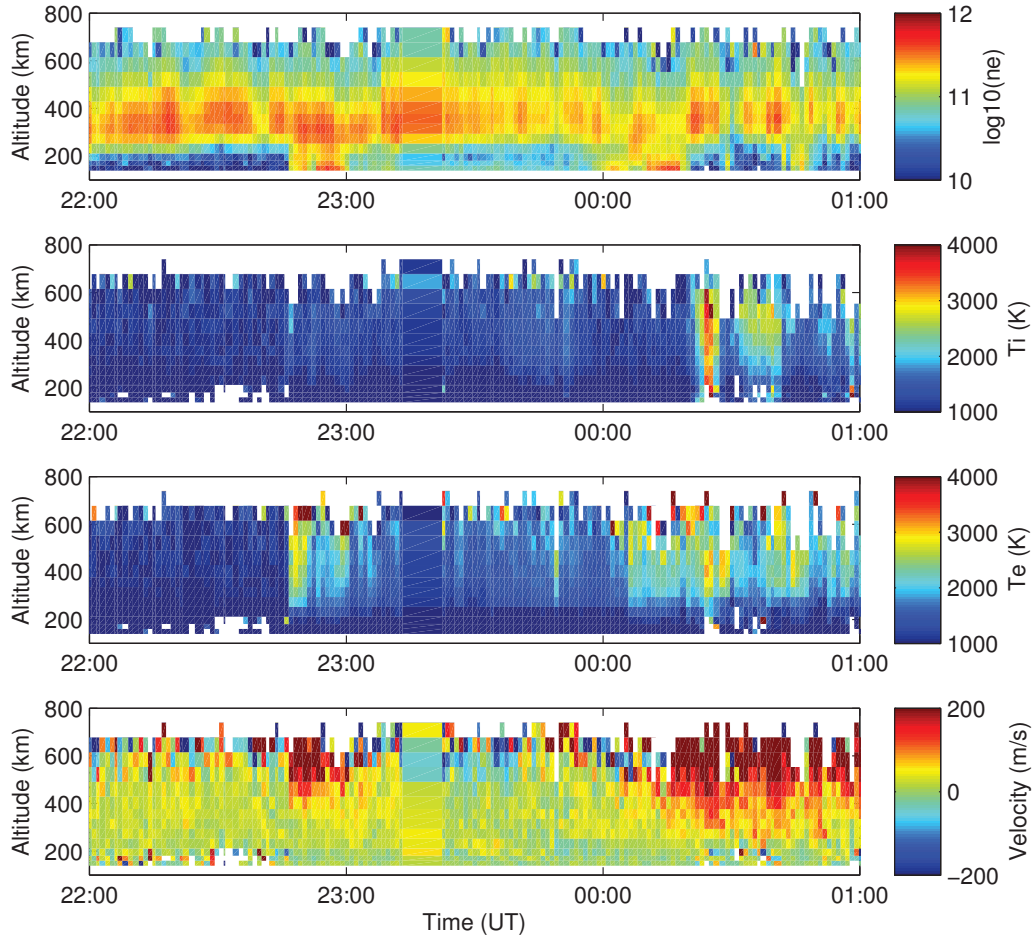
Figure 4.9: Sondrestrom radar data from 12/07/1999. A type 2 upflow event is observed at 22:40 UT; high velocities in panel 4 correspond with an increase in low altitude densities and electron temperatures. There is also a type 1 upflow event at 0:25 UT; high velocities correspond with a large increase in ion temperature.

The velocity is larger than 100 m/s for altitudes greater than 300 km and larger than 200 m/s at altitudes higher than 550 km (panel 4). There is not an increase in low altitude density (panel 1) for the E-region. These type 1 and type 2 events within this

dataset are typical examples and results from the force balance analysis and steady state velocity calculation mirror the results from the previously discussed upflows.

4.2   Neutral Wind Events

While examining and categorizing the 61 events listed in Table 3.2, four events did not fall within the type 1 or type 2 categories. Two events did not contain any heating signatures and two did not exhibit the previously defined features marking a type 1 or type 2 upflow. In the following datasets, the upward flowing velocity is initiated/present at low altitudes, 200-400 km, instead of 400-600 km and/or there is not an associated increase in ion or electron temperatures above background conditions. For these non-categorized data sets, evidence suggesting neutral wind uplifting of the ionosphere as the driver of the upflow is presented. Several mechanisms are suggested and include gravity waves, solar forcing and ion-neutral coupling.

4.2.1   Neutral Wind Event 1

ISR data from 12/04/1999, Figure 4.10, has the peculiar upflow velocity signature suggestive of the influence of neutral winds. All of the observed upward velocities (panel 4) are at low altitudes and do not continue throughout the radar range. This creates a distinctive "pod" shape of upflowing ions. The continuously high electron temperatures (panel 3) are due to the daytime nature of the observation. Electrons created by UV radiation have excess energy and thermalize with the background ionospheric electrons, raising their temperature. There is a co-occurring type 1 upflow event at 16:07 UT with highly elevated ion temperatures (panel 2) that temporarily
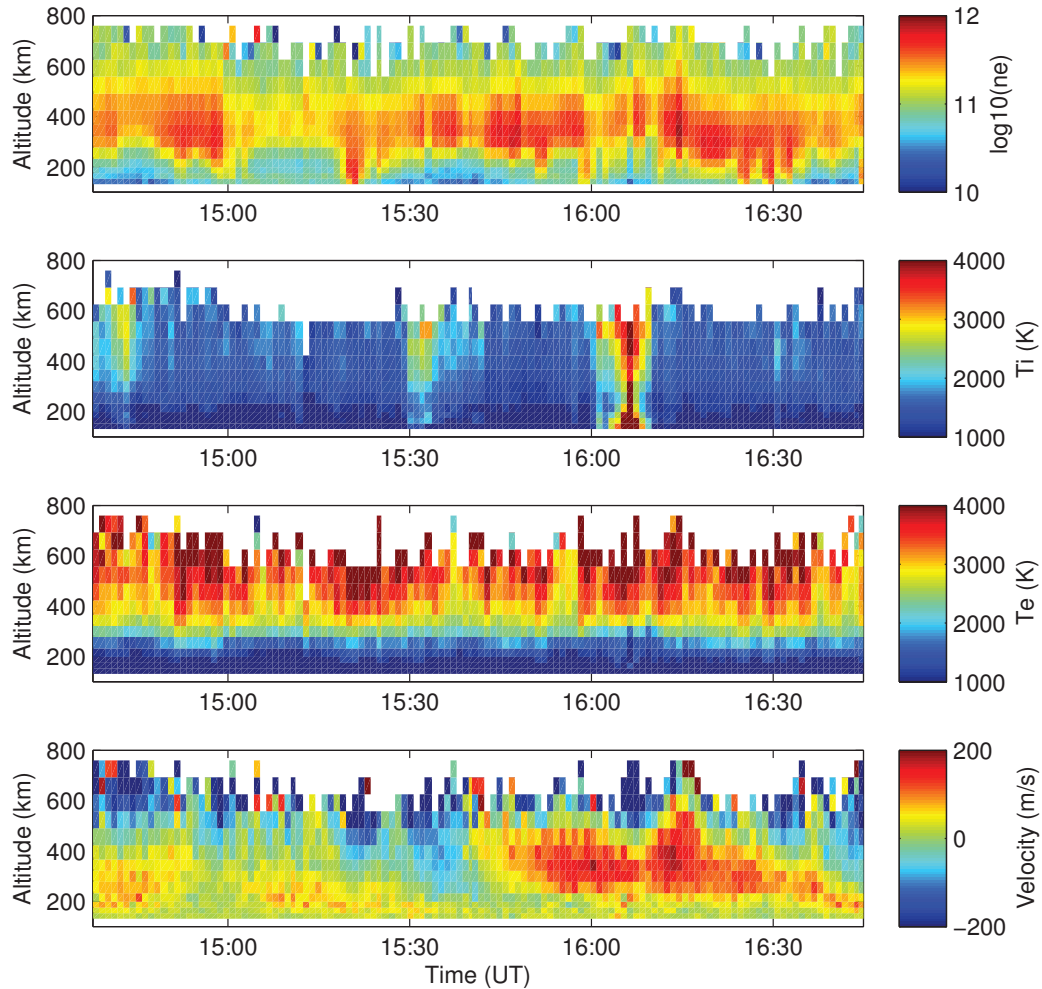
Figure 4.10: The observed electron density, ion temperature, electron temperature and line of sight velocity from the ISR on 12/04/1999 at Sondrestrom.

decreases the ion velocity.

By applying Equation 2.10 to the collected ISR data the four forces of interest are calculated. The forces, in individual panels, are presented in Figure 4.11. These
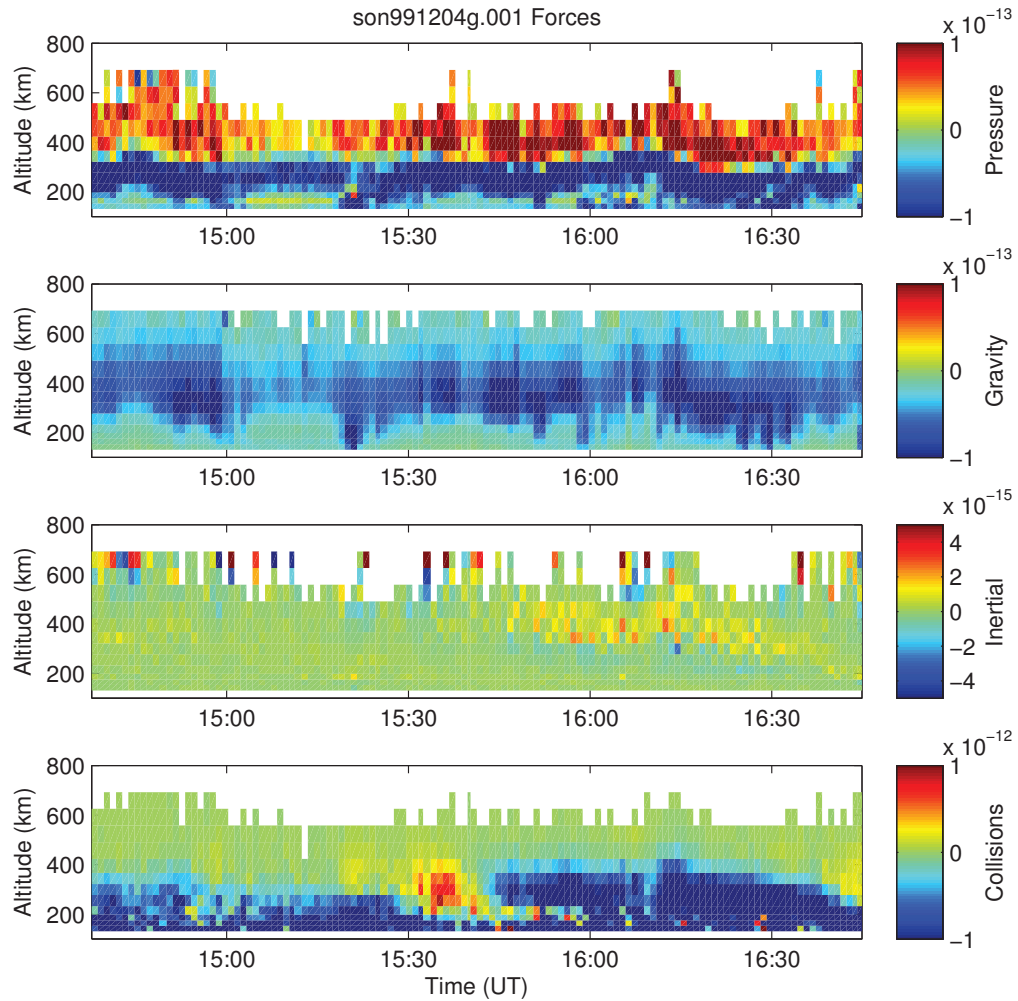
Figure 4.11: The calculated forces acting on the plasma from the data collected on 12/04/1999 at Sondrestrom.

panels are top to bottom: the pressure gradient, gravitational forces, inertia, and collisional forces. The pressure gradient is split along the F-region peak as expected. The effects of gravity are larger in places of high density. Inertia is several orders of magnitude smaller than the other forces. Collisional effects dominant the calculated

forces and act in the direction opposite of the observed velocity.

Calculating the steady state velocity, for this dataset collected on 12/04/1999, with Equation 2.13, Figure 4.12 is created. The top panel is the calculated steady state velocity, the middle panel is the observed velocity and the bottom panel is the estimated neutral wind component of the observed velocity. During the steady state calculation the neutral wind is assumed to be negligible. For some cases, like this one, that assumption is not particularly valid. Subtracting the calculated steady state velocity from the observed velocity gives an approximation for the neutral wind.

Figure 4.12: The calculated steady state velocity, top panel, the observed velocity, middle panel, and the estimated neutral wind for part of 12/04/1999 at Sondrestrom.

This estimation matches very well with the observed velocity both in strength and location. At 300 km, the estimated neutral winds range from approximately 40 m/s up to a max velocity of 200 m/s. Suggested neutral wind velocities, by King and Kohl (1965) and Rishbeth and Garriott (1969), at 300 km, are between 30-100 m/s and may reach up to 300 m/s during storm conditions. These speeds agree with the estimated neutral winds calculated from the observed upflow event.

4.2.2 Neutral Wind Event 2

The second, non-categorized upflow event occurred on 05/31/2003 at Sondrestrom. The electron density, ion temperature, electron temperature and observed velocity are presented in Figure 4.13. In the observed velocity (panel 4), the low altitude regions (200-400 km) contains periodic, upward velocities. The period is roughly 50 minutes with velocities averaging 50 m/s per perturbation with some stronger occurrences that reach speeds up to 200 m/s. These periodic upflows have a downward phase progression extending in altitude down to 200 km, well below the standard altitude range of type 1 and type 2 upflows. The ion temperature (panel 2) throughout this data set is minutely elevated occasionally but not in response to any of the observed upflows. The electron temperature (panel 3) also does not respond to any of the periodic upflows and appears to be unaffected by them.

The calculated forces from the force balance analysis, Figure 4.14, exhibit standard responses with the exception of the collisional forces (panel 4). The periodic signature seen in the observed velocity also appears in the collisional forces; as the plasma periodic motions serve to change the directions in which the collisions are acting.
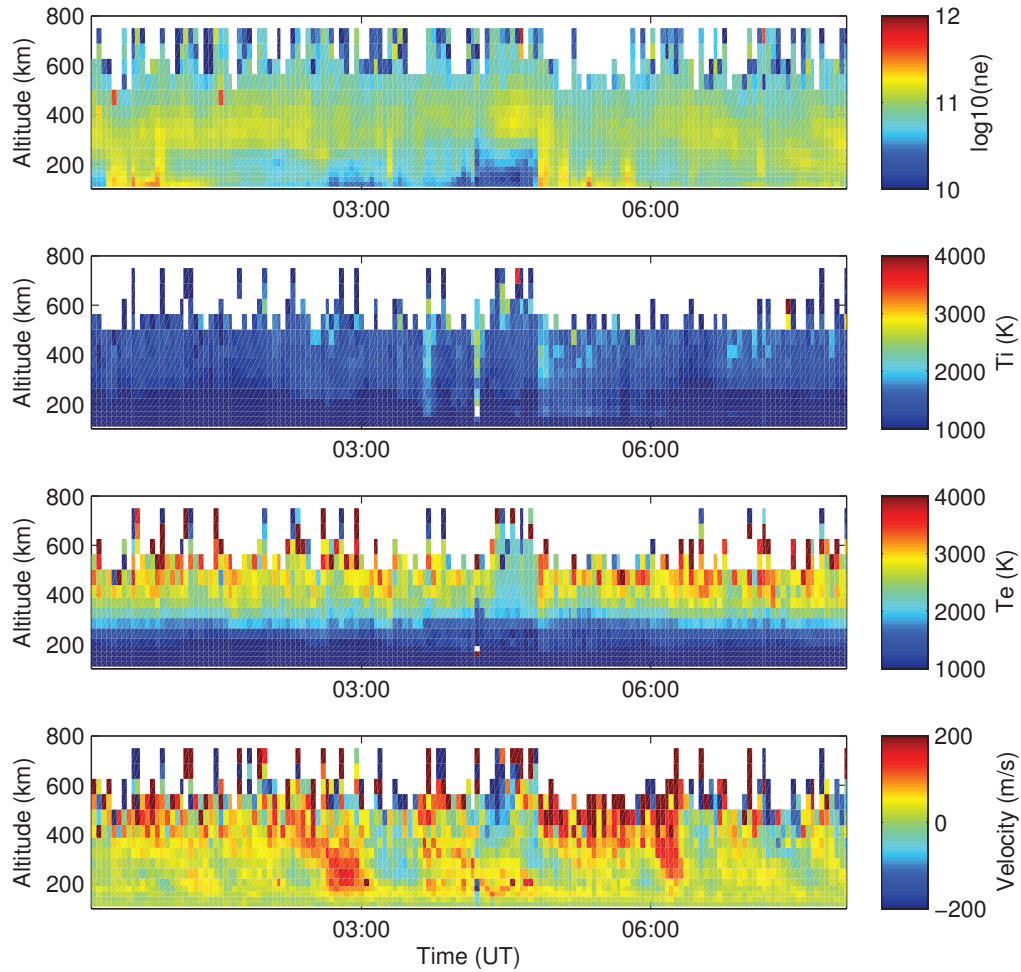
Figure 4.13: Observations of low altitude, periodic upflows on 05/31/2003.

The calculated steady state velocity, top panel of Figure 4.15, doesn't have many indications of upflowing ions compared to the observed velocity, middle panel. When the steady state velocity is subtracted from the observed velocity an estimate for the neutral winds is found, bottom panel. This estimate matches well with the observed
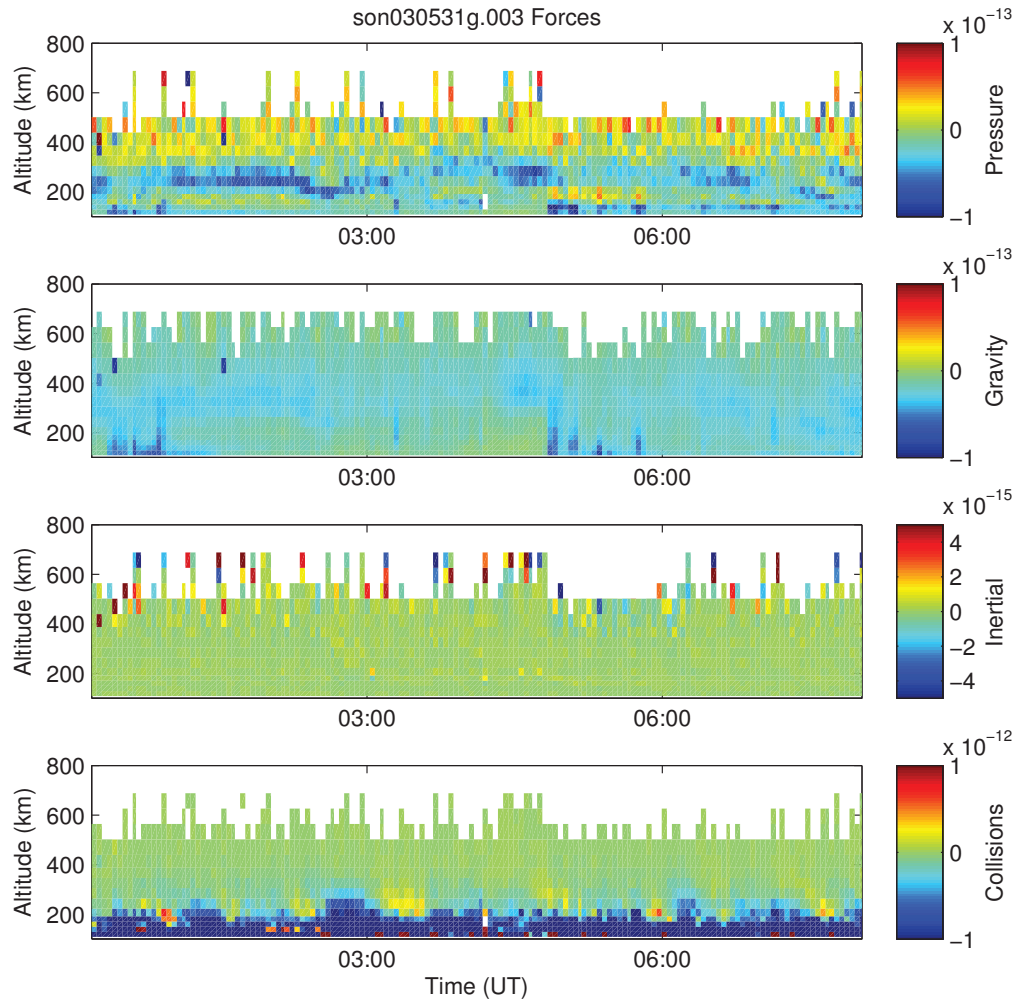
Figure 4.14: The calculated forces acting on the ionospheric plasma on 05/31/2003 at Sondrestrom. The periodic signature seen in the observed velocity also appears in the collisional forces (panel 4).

velocity, even down to the periodic structures of upflow times. The short periodicity of the low altitude upflows as well as the downward phase progression supports this being an observation of a gravity wave (Hunsucker, 1982; Kelley, 2009).
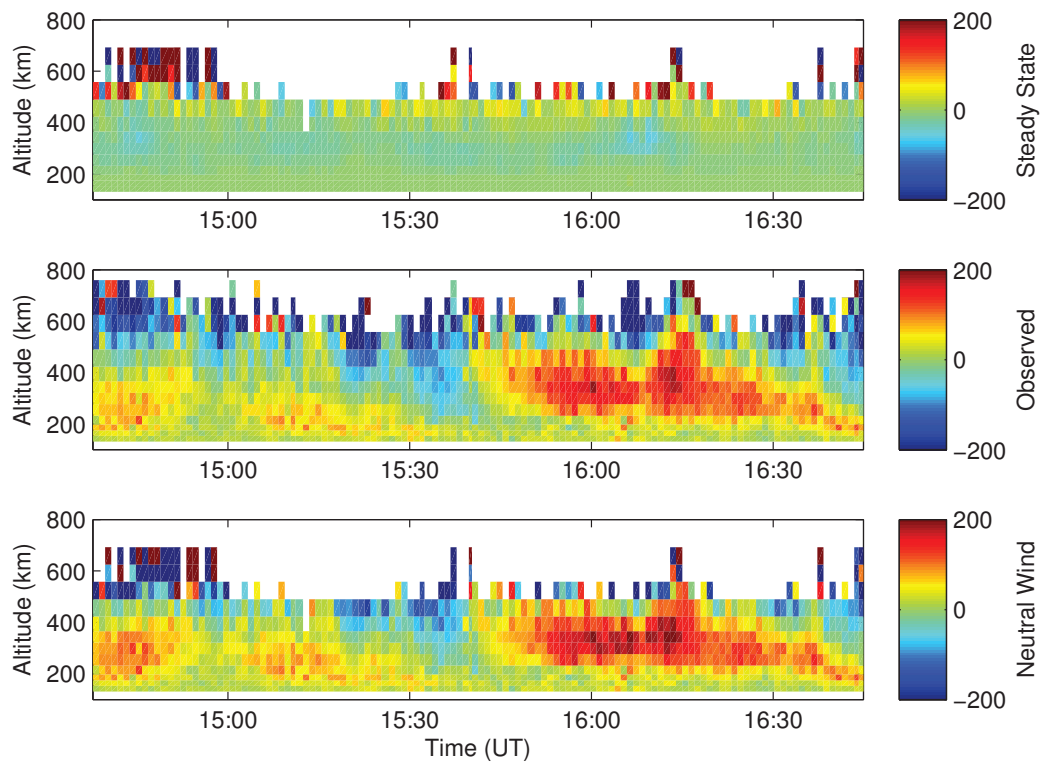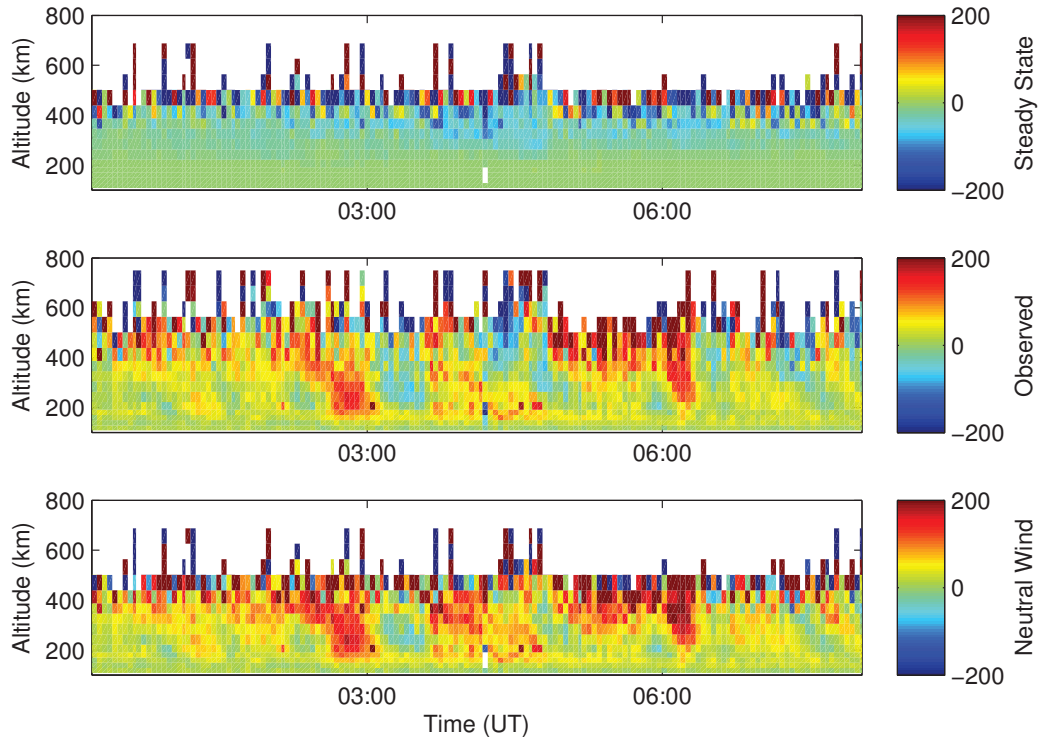
Figure 4.15: The calculated steady state velocity, top panel, the observed velocity, middle panel, and the estimated neutral wind for part of 05/31/2003 at Sondrestrom.

4.2.3   Neutral Wind Event 3

The third, non-categorized upflow event was observed on 06/24/2003 at Sondrestrom using the ISR. The electron density, ion temperature, electron temperature and observed velocities from this dataset are presented in Figure 4.16. The extended observational time, lasting 48 hours, gives the benefit of being able to search for upflow trends with extended periodicity. The electron density (panel 1) increases during the day due to the photoionization of the ionosphere and dramatically decreases at night from recombination. The ion temperature (panel 2) at approximately 9:00 UT on the
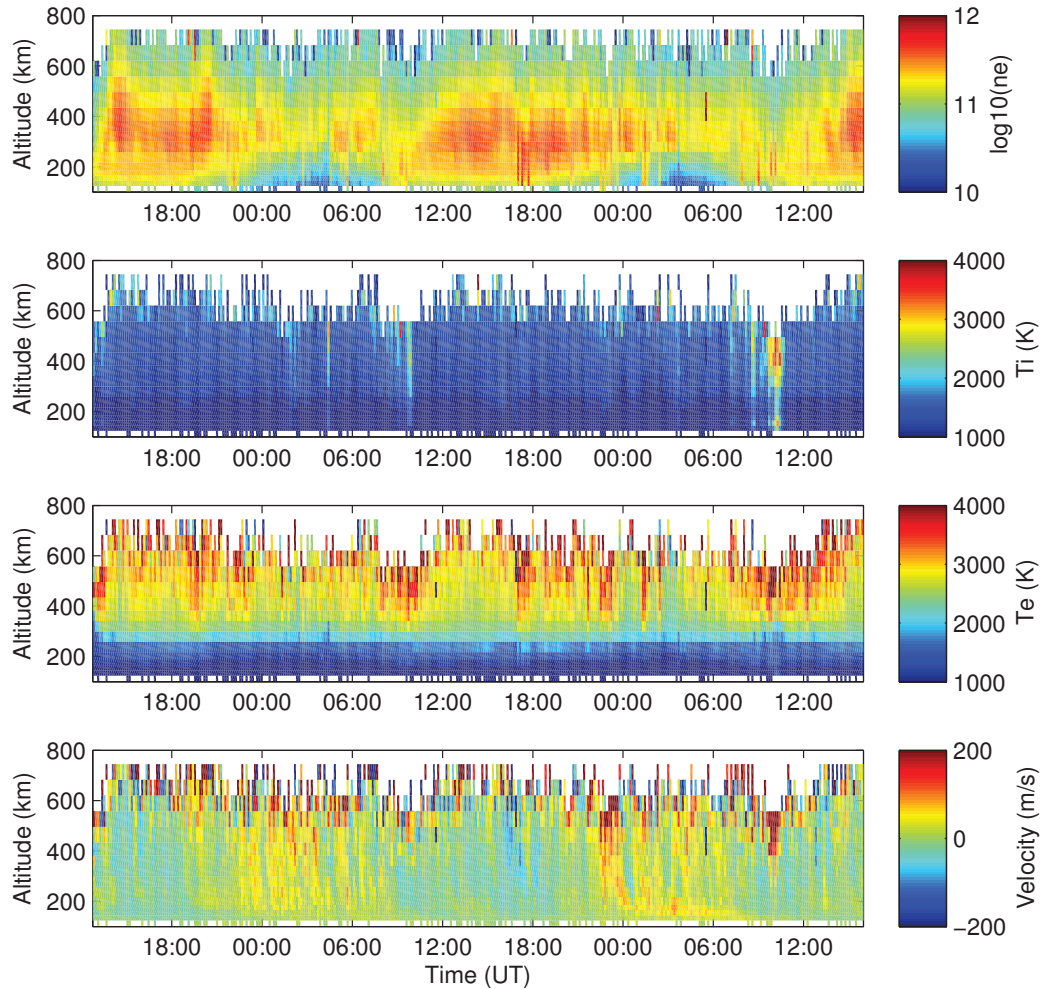
Figure 4.16: The electron density, ion temperature, electron temperature and line-of-sight velocity from the ISR at Sondrestrom from 06/24/2003 to 06/26/2003.

third day has a large, short term, increase in the ion temperature that corresponds to an increase in the observed velocity indicating a strong type 1 upflow event. Other than that there are no significant increases in ion temperature. The electron temp-

eratures are consistent throughout the majority of this dataset (panel 3). The upflows (panel 4) extend over a large altitude range, from 200 km up to greater than 600 km. These upflows repeat, from 22:00 UT to 7:00 UT for each day within this observation.
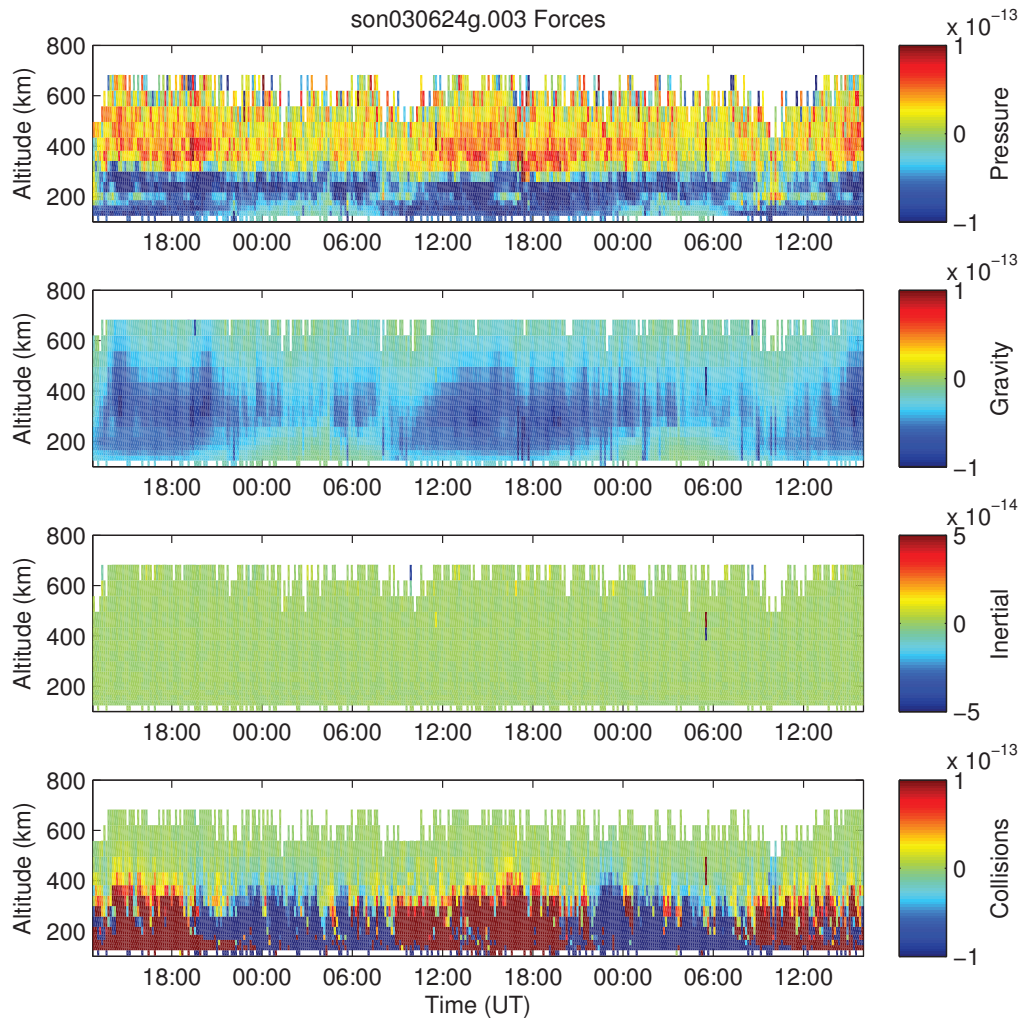
Figure 4.17: The calculated forces acting on the ionospheric plasma for 06/24/2003 to 06/26/2003 at Sondrestrom.

Using this data in the force balance analysis yields the four forces plotted in Figure 4.17. Once again the calculated forces exhibit standard responses with the exception of the collisional forces (panel 4). The periodic signature seen in the observed velocity also appears in the collisional forces. The nightly upflows correspond to the highly negative collisional forces seen most strongly at lower altitudes.
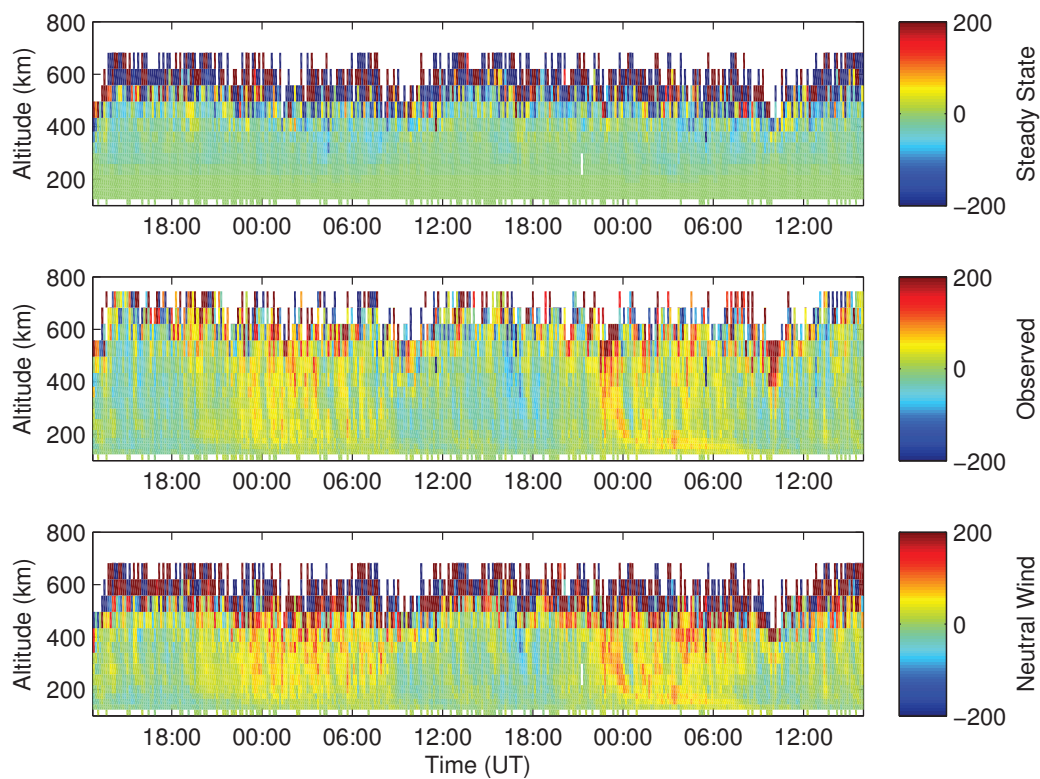
Figure 4.18: The calculated steady state velocity, line of sight velocity and the estimated neutral wind for 06/24/2003 to 06/26/2003 at Sondrestrom.

Using the data from 06/24/2003 to 06/26/2003, a steady state velocity calculation yields the information presented Figure 4.18. The steady state velocity (panel 1) is calculated for all of the altitudes that there is data for; in altitudes greater than 450

km, it can be seen that these calculation tends to produce extreme velocities. This suggests that the steady state assumption is not always accurate above 450-500 km. This potential limitation is also seen in the estimated neutral wind (panel 3) which is calculated from the difference between the observed velocity (panel 2) and the steady state velocity. At low altitudes the neutral wind estimation still matches well with the observed velocities.

A suggested cause for the estimated neutral winds is solar forcing. From the influence of EUV and Xrays a pressure differential is created between day and night sides of the atmosphere. As a result, there is atmospheric flow from the high pressure, day side to the low pressure, night side. This would create velocity components, parallel to the magnetic field lines, that are negative during the day and positive at night echoing the upflows seen in this radar data. The solar forcing effect would be largest at solar max and minimal around solar min. With this observation taking place just after solar max it is plausible that the source of the estimated neutral winds is solar forcing. To achieve the estimated 50 m/s field aligned winds, a geographic poleward wind of approximately 250-300 m/s is necessary.

4.2.4 Neutral Wind Event 4

The fourth non-classified upflow event occurred on 07/26/2004. This event contains two periods of observed velocities upwards of 150 m/s at altitudes as low as 200 km (panel 4). These last for several hours, primarily between 0:00 UT and 6:30 UT as seen in Figure 4.19. The ion temperatures (panel 2) are minimally raised, not enough to create thermal expansion, throughout this time. The electron temperature (panel 3) is not raised significantly above background conditions for the majority of this
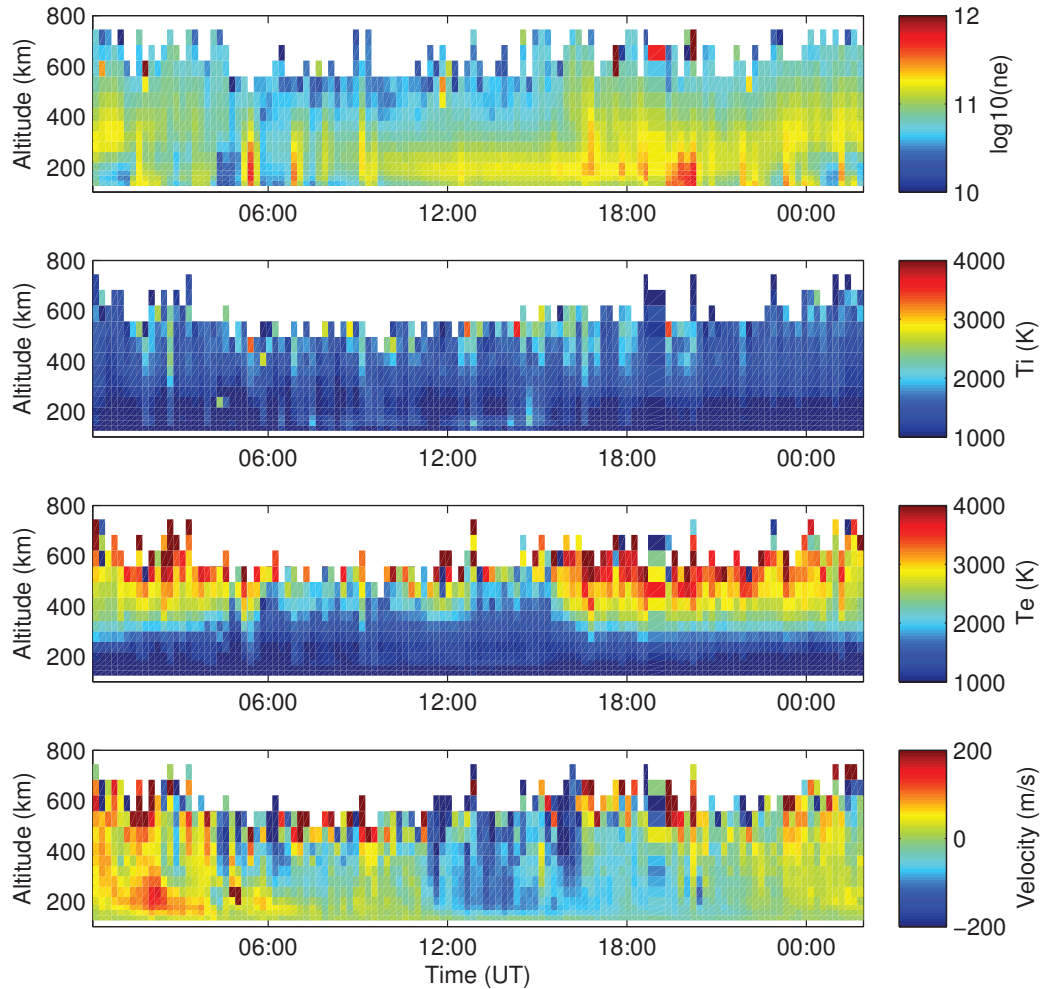
Figure 4.19: Observations from 07/26/2004 to 07/27/2004 at Sondrestrom. The electron density, ion temperature, electron temperature and line of sight velocity from the ISR data are presented.

time frame though for a portion of the day they do decrease when the F-region peak decreases in altitude. This lowering of the peak density altitude is caused by the storm conditions. The k_p index is fluctuating between 7 and 8.7 during this time.
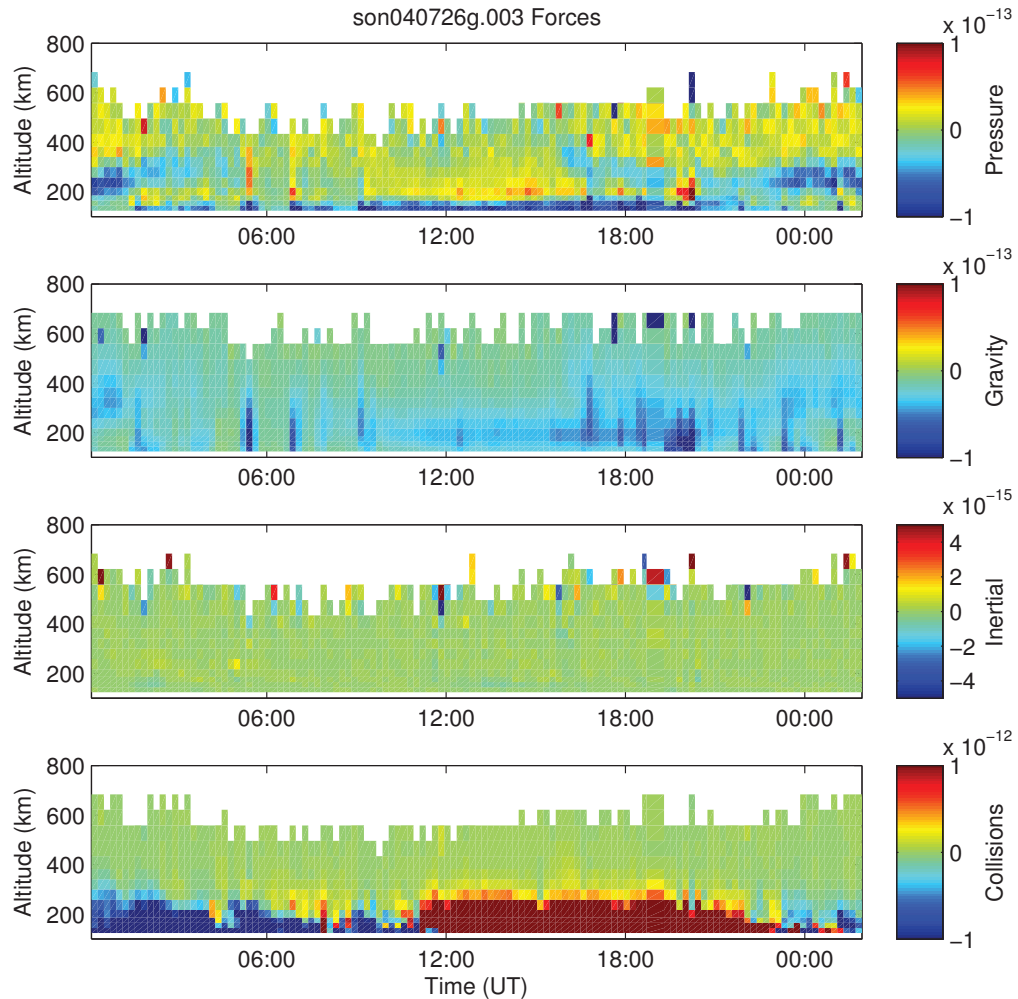
Figure 4.20: The calculated forces acting on the ionospheric plasma for 07/26/2004 at Sondrestrom. These include the effects from the pressure gradient, gravity, inertia and collisions between the ions and neutrals.

Using the observation data with the force balance analysis, Equation 2.10, the four panels in Figure 4.20 are created. The pressure gradient (panel 1) is not clearly aligned through time but this is due to the unusual altitudinal dip in peak densities during the

day from storm conditions. Gravitational forces and inertia exhibit standard trends. The collisional forces (panel 4) are most strongly felt and consistently act against the direction of ion flow. The lower ionosphere should be in a case of steady state with all of the forces balancing and becoming equal. This is not the case for most of the events discussed within this Chapter suggesting that either a) the neutral wind needs to be taken into account in the force balance calculation (instead of assuming it is zero) or b) there are other unaccounted for forces affecting the system.
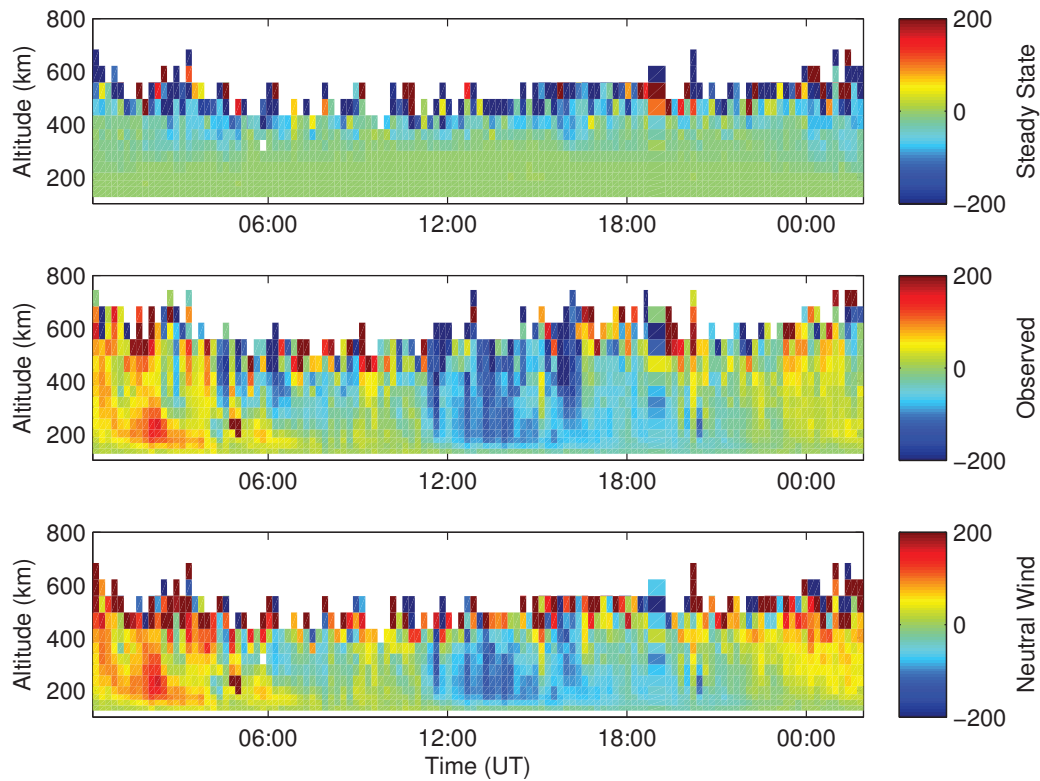
Figure 4.21: The calculated steady state velocity (panel 1), the observed line-of-sight velocity (panel 2), and the estimated neutral wind (panel 3) for 07/26/2004 from Sondrestrom.

Calculating the steady state velocity, using Equation 2.13, for 07/26/2004 produces panel 1 of Figure 4.21. The observed velocity (panel 2) is included again for comparison purposes. The calculated steady state velocity does not capture the dynamical features of the observed velocities suggesting neutral wind influence. The bottom panel is the estimated neutral wind obtained from subtracting the steady state velocity from the line of sight velocity.

While the occurrence times of the up and down flows correspond to night and day, like with the previous suggested case of solar forcing, these upflows contain more low altitude action. Ion-neutral coupling occurs at high latitudes when the ions, which typically follow a two cell convection pattern, impart momentum to the neutrals from their motions. The previous and current storm conditions create a lot of energy and action within the ionosphere. This action is imparted to the neutrals to such a degree that the observed upflows may be impacted by this type of neutral wind.

Chapter 5

MODELING THE IONOSPHERE

5.1 An Ionospheric Model

Ion upflow is not always adequately described by the force balance and steady state equations used previously. These equations do not capture and describe transient effects, nonlinearity and complicating factors like heat flux. A numerical model is needed to describe in fuller detail these additional processes. The model, GEMINI, used for this study utilizes a fluid transport description of the multi-species ionospheric plasma and describes the plasma in terms of the species number density, n_s, the drift velocity, $\vec{v}_s$, and pressure, p_s (Zettergren and Semeter, 2012; Schunk, 1977). Seven species of ions are considered within this model: $O^+, NO^+, N_2^+, O_2^+, N^+, H^+$ and e^-. A set of fluid conservation laws, outlined below, are solved for each species.

The continuity equation describes the transportation of mass and how the densities of the different species are controlled by chemical production and loss, photoionization

via solar EUV and Xray radiation, as well as by impact ionization,

$$\frac{\partial n_s}{\partial t} + \nabla \cdot (n_s \vec{v}_s) = P_s - L_s n_s. \tag{5.1}$$

P_s is the production processes and L_s is the loss processes.

The ion drift velocities are described by the momentum equation. Within this model, the form of the momentum equation is modified slightly from Equation 2.8.

$$
m_s \left(\frac{\partial \vec{v}_s}{\partial t} + \nabla \cdot (\vec{v}_s \vec{v}_s) \right) = m_s \vec{v}_s (\nabla \cdot \vec{v}_s) + m_s \vec{G} - \frac{1}{n_s} \nabla \vec{p}_s
$$
$$
+ q_s \left(\vec{E} + \vec{v}_s \times \vec{B} \right) + \sum_n m_s \nu_{sn} (\vec{v}_n - \vec{v}_s) \tag{5.2}
$$

The partial pressure is given as $\vec{p}_s = n_s k_b \vec{T}_s$ where k_b is the Boltzmann constant.

The energy of the plasma, written in terms of the temperature and with an added term to account for the heat fluxes, is written as,

$$
\frac{\partial T_s}{\partial t} + \nabla \cdot (T_s \vec{v}_s) = \frac{1}{3} T_s (\nabla \cdot \vec{v}_s) - \frac{2}{3 n_s k_b} \nabla \cdot \vec{h}_s
$$
$$
- \sum_n \frac{m_s \nu_{sn}}{m_s + m_n} \left(2(T_s - T_n) - \frac{2}{3} \frac{m_n}{k_b} (\vec{v}_s - \vec{v}_n)^2 \right), \tag{5.3}
$$

where $\vec{h}_s = -\lambda_s \nabla T_s$ and $\vec{h}_e = -\lambda_e \nabla T_e - \beta_e \vec{J}$ (Zettergren and Semeter, 2012; Schunk, 1977). This latter form of the equation takes into consideration both thermoelectric effects and thermal conduction. The thermal conductivity for ion species s is λ_s. λ_e and β_e are the electron thermal conductivity and thermoelectric coefficients respectively (Schunk and Nagy, 2000, p. 132). The heat flux in this case is assumed only along the magnetic field lines.
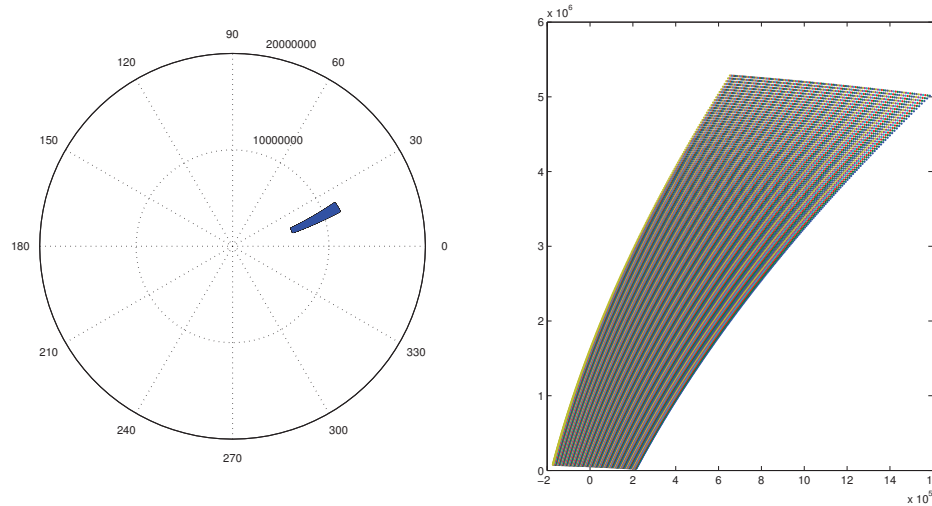
Figure 5.1: The top down view of the location of the dipole mesh used within the model [left]. A side-on view of the same mesh [right]. The number of field lines and altitude devisions are adjustable for the precision and calculation speed desired.

The neutral densities necessary for calculating the reaction rates and collision frequencies in this model for the production and loss terms are taken from NRL-MSISE-00 (Picone et al., 2002). Chemical reactions considered within this model are from Diloy et al. (1996) and St. Maurice and Laneville (1998). Photoionization calculations for the the dayside are from Solomon and Qian (2005). All equations are resolved on a 2D dipole mesh that emulates the structure of Sondrestrom's local magnetic field lines to a high degree. The number of field lines used and the number of cells along the field lines are customizable to facilitate optimization of calculation speeds. Some of the numerical methods employed include a split operator approach for the advection, source/loss and diffusion equations, the Lax-Wendroff or slope/flux-limited FVM for hyperbolic systems, exponential time differencing for source/loss processes and a 2nd order backward difference trapezoidal integration for intermediate

diffusion steps (TRBDF2).

Within the model the main controllable parameters include precipitating electrons, background currents, electric potentials, and/or neutral winds that can be arbitrarily specified in both strength and location of application. Using this complex model the effects of frictional heating, plasma expansion/upwelling, horizontal advection, and auroral currents will be explored for cause and effect relationships as well as determining observable identifiers of physical processes.

5.2 Modeling Ion Upflow Events in the Ionosphere

In order to corroborate the observed ion upflows features, simulations of different sources of ion upflows were created. For this study, possible effects of upflows produced by type 1, type 2, neutral wind and density cavity driven upflows are considered and the unique characteristics of each can be compared to features of ISR observations. Initiating the model required creating steady state initial condition. By running the ionosphere model for several model days without added influences, the ionosphere will reach dynamic equilibrium. This equilibrium is necessary when developing energy and upflow signatures in order to avoid creating extra features from unphysical transients due to out-of-equilibrium initial conditions. It should be noted that the ionospheric model used here, called GEMINI, automatically takes into consideration photoionization effects from the sun. This creates a natural "breathing" action in the ionosphere due to photoionization and photoelectron heating that depends on time of day and where the peak density altitude is located. Reproducing this real world phenomenon helps to make the simulations more accurate and does not induce unphysical fluxes disruptive to the created upflows. A very small amount of "background" precipitation

at 500 eV, much smaller than any induced precipitations driving upflow conditions at 0.1 mW/m^2, is also set to further emulate real world conditions.

The model simulations encapsulate the two main types of ion upflows as well as neutral wind and cavitation simulations. Table 5.1 contains summary information about the models presented within this Chapter. As seen in the ISR data, the length of time that observed ion upflows last is variable but 7.5 minutes is a rough average of the observed durations. For the type 1, type 2 and neutral wind simulations, perturbation creating sources were applied for 7.5 minutes and then turned off. This creates disturbances that propagate for another 15 minutes (22.5 minutes for the type 2 upflow simulation) for a total of 22.5 simulated minutes (30 minutes for the type 2 upflow). The cavitation model runs were created by using a 2D Gaussian shaped well in the density profile for the initial conditions and ran for a total of 22.5 simulation minutes. The strength of these upflow driving sources were selected to best show the upflowing features. GEMINI can process much larger and longer perturbations than any found within the examined ISR data and still retain coherency within the calculations.

Table 5.1: A summary of the presented simulations of ion upflows within this Chapter.

Simulation	Upflow Driving Source	Peak Strength
Type 1	Electric Potential	110 mV/m
Type 2	Electron Precipitation	4 mW/m^2
Neutral Wind	Neutral Wind	75 m/s
Cavitation	Density Cavity	50% depletion

The shape of the applied upflow source is designed as a Gaussian distribution to capture the 2D nature of a region of upflowing ions. This distribution is centered

around the middle field line of the simulation, Figure 5.1, making the induced distur-
bance distant enough from the edges of the simulated space to be unaffected by the
lateral boundary conditions.

Table 5.2: The distribution equations used when applying the different types of upflow
sources.

Simulation	Distribution Equation
Type 1	peak$*$erf$((xg.x2 - x2ctr)/delx2)$
Type 2	peak$*$exp$(-(xg.x2 - x2ctr)^2/(sigx2)^2)$
Neutral Wind	-62.5(tanh(altitude-130/80))-62.5
Cavitation	exp$(-((x1 - x1(x1p))^2)/sigx1^2)*exp(-((x2 - x2(x2p))^2)/sigx2^2)$

After a simulation in 2D is run, the center field line is selected for further analysis
with the force balance and steady state velocity calculations. This is analogous to,
and captures the limited scope of, the single beam of the ISR. One benefit of using
GEMINI is that multiple ion species are considered allowing for O^+ and H^+ to be
looked at individually from the results of the simulations. For the actual radar data,
the ionosphere is assumed to be just O^+ as there isn't a good way to separate out
more ion information without making many additional relationship assumptions. The
model is fully time-dependent and nonlinear allowing for all ion propagation speeds
to be determined.

5.2.1 Modeled Type 1 Upflows

Type one upflows, driven by frictional heating, are created using some of the ad-
justable parameters build into GEMINI. Multiple model runs of type 1 upflows at
various strengths were conducted but because they all had the same upflow signa-
tures one is described in detail. To create a type 1 upflow an electric potential was

applied for the first 7.5 minutes of the simulation and the system was allowed to propagate afterwards. This initial excitation period creates an upflow that continues to propagate upward long after the source is removed. The type 1 upflow simulation discussed below has a target electric field peak of 110 mV/m produced along
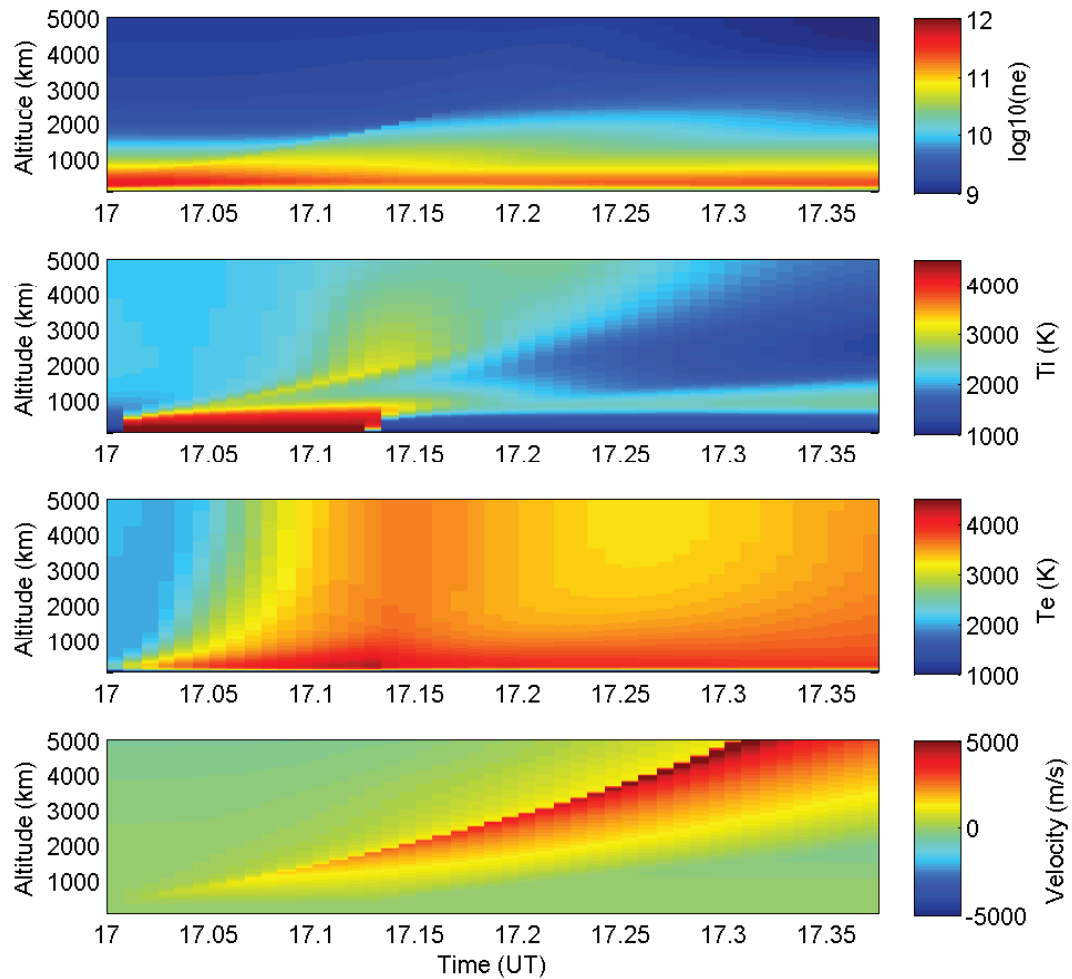

Figure 5.2: A modeled type 1 ion upflow with an electric potential target peak of 110 mV/m and a stimulation duration of 7.5 minutes.

the center field line. The values for the electron density, ion temperature, electron temperature and O^+ velocity are presented in Figure 5.2 and contain several notable and distinctive features.

For the total duration of the simulation the region of ion upflow (panel 4) continuously propagates upwards. The response is not instantaneous over all altitudes when there is an applied energy source though that is a common simplification used when describing the ionosphere. The applied electric potential creates frictional heating and increases ion temperature (panel 2) at lower altitudes from 17.0-17.125 UT. As the ion temperature is increased the ability of the ions to undergo heat exchange with the electrons is decreased as they are closer to thermal equilibrium. Because the ions cannot act as a heat sink for the electrons (which are still getting heated by photoionization during this time of day) the electron temperature increases, even above the ion temperature, for these low altitudes and time (panel 3). Through frictional heating and the high thermal conductivity of the electrons an increase in electron temperature up to 3500 K is quickly propagates upwards in altitude even before the stimulation is turned off. This can pave the way for increasing the propagation speeds (by creating a warmer region to propagate through) and the spreading of the heat initiates upflows more quickly at high altitudes. The upflowing ions, (panel 4), act to lift the ionosphere creating, by 17.2 UT, a clearly uplifted density (panel 1). The uplifting process is responsible for compressionally heating the ions from 17.12-17.2 UT at altitudes above the upflow and outside of the normal range of any ISR. In the latter portion of the simulation there are downflowing ions from the relaxation and passing of the upflow to higher altitudes. Expansive cooling also is occurring at the higher altitudes. The downflow results in the compressional heating seen in

the 800 km to 1800 km range in the ion temperatures (panel 2) from 17.4 to 17.5 UT. It should be noted that another of the advantages of the model is the extended altitude range of the data. Radar data is limited to a maximum height between 400 km and 1000 km. GEMINI, as used here, calculates up to 5000 km. This allows for
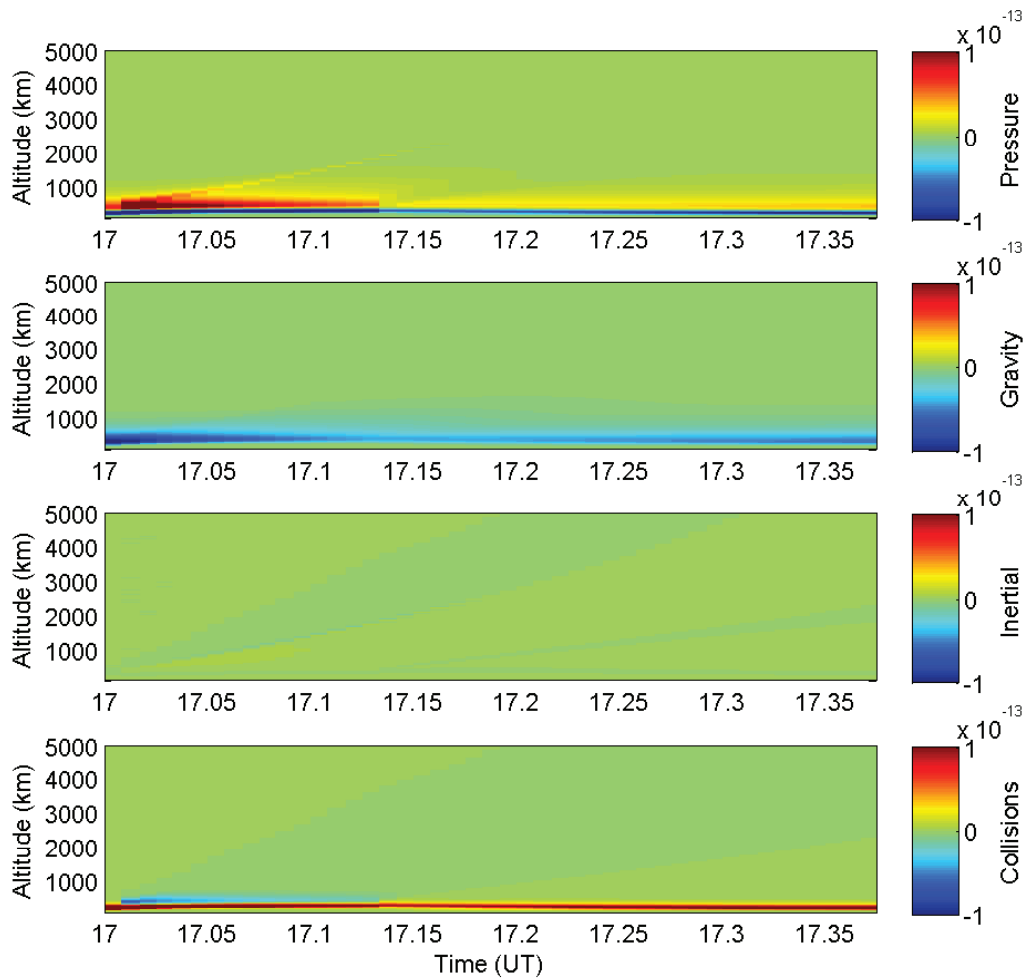

Figure 5.3: The calculated forces from the type 1 simulation. The model GEMINI allows for a much larger altitude range to be examined than the range of standard ISR data.

the disturbances to propagate to higher altitudes and not be numerically interfered with by the top boundary conditions.

The force balance calculation can be applied to simulated upflows as well and for the type 1 simulation produces the four forces plotted in Figure 5.3. The forces are, once again, the pressure gradient, gravitational forces, inertia and collisions. As the altitude increases, the density of the atmosphere decreases exponentially and the forces become very very small. At lower altitudes, in the region where the radar is detecting, the model features match with the radar data features; there is the positive pressure gradient above the peak density region and the negative pressure gradient below, gravitational forces are greatest in regions of highest density, inertia is super small and the collisional forces, in general, act in the direction opposite of the velocity of the ions.

The sum of these forces is presented in Figure 5.3. This sum is very close to equilibrium for most time steps and altitudes supporting the steady state nature of the ionosphere that the model is based on. During the build-up period of the simulation the sum of the forces does deviate from equilibrium at low altitudes and the leading edge of the initial upflow is also not in a steady state equilibrium.
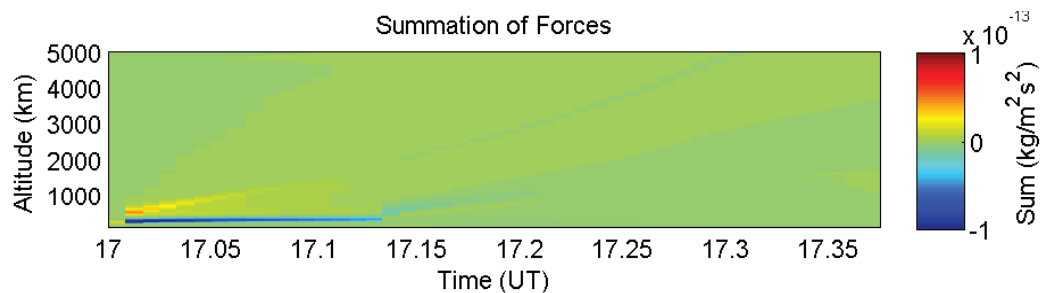
Figure 5.4: The summation of the calculated forces from the type 1 modeled ion upflow event.
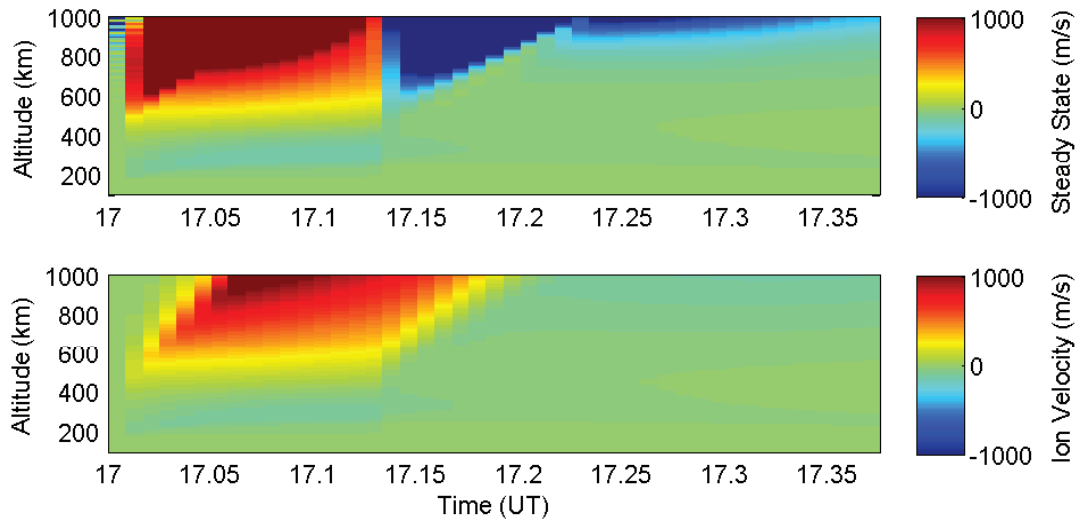
Figure 5.5: The calculated steady state velocity (top panel) from the type 1 modeled ion upflow event for the altitude region observable by ISR. The actual velocity (bottom panel) is included for comparison.

Using the forces in Figure 5.3 the steady state velocity is calculated for the modeled type 1 event. Zooming in to the altitude region that is observable by Sondrestrom's ISR, the steady state velocity and O^+ velocity are presented in Figure 5.5. The steady state velocity (panel 1), calculated from Equation 2.13, has a good agreement with the ion velocity (panel 2) in the lower regions. At higher altitudes (>600 km) the steady state velocity is grossly over or under estimated. This same trend was seen in the radar data's steady state velocity calculations. There is a direct correlation between the acceleration/deceleration of the ions and where the steady state velocity was over/under estimated respectively.

5.2.2 Modeled Type 2 Upflows

Type 2 ion upflows are created in GEMINI by applying Maxwellian electron precipitation with a characteristic energy of 500 eV and result in an increase in low altitude

Figure 5.6: A modeled type 2 upflow event. The peak electron precipitation is simulated at 4 mW/m^2 with a stimulation duration of 7.5 minutes.

electron density and electron temperature. Multiple model runs were completed of type 2 upflows, for a plethora of strengths, and the main features of all of the type 2 simulations were the same. A type 2 simulation lasting 30 minutes with a peak electron precipitation at 4 mW/m^2 for the initial 7.5 minutes is presented 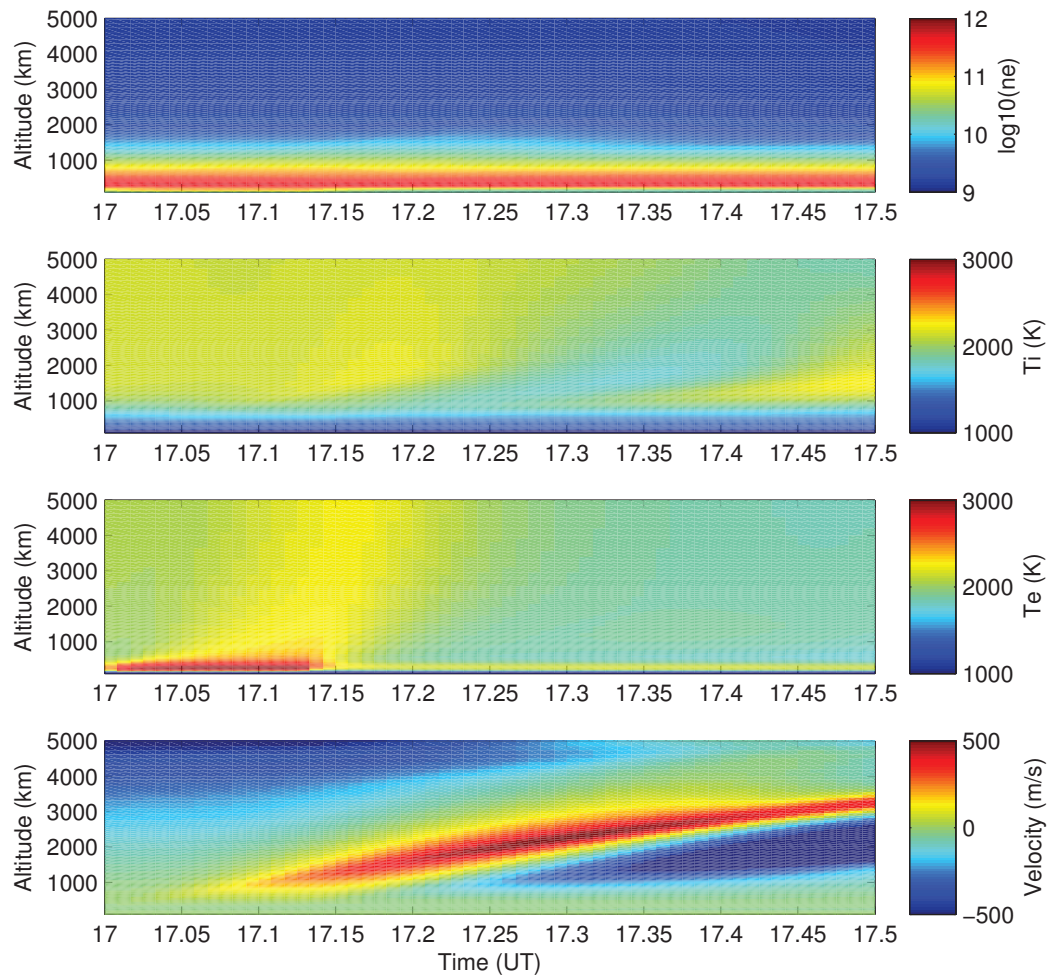in Figure 5.6. The four panels, in descending order, include the electron density, ion temperature, electron temperature, and O^+ velocity. The simulated precipitating electrons cause the increase in electron density (panel 1) and temperature (panel 3) in the 200-300 km range from 17 UT to 17.13 UT. The high thermal conductivity of the electrons heat the region above the original thermal increase as time progresses. A minor increase in ion temperature (panel 2) from 17.14 UT to 17.25 UT is due to heat transfer from the electrons. The initial 2000-2300 K ion temperatures seen from 17 UT to 17.1 UT are due to photoionization. The overall increase in energy and temperature acts to loft the ionosphere up creating the increase in density seen best around 1700 km, centered at 17.25 UT (panel 1). Once the lofted ionosphere begins to settle, compressional ion heating is created from 17.4 UT onwards (panel 2). Throughout all of this, the ion upflow continues to propagates upwards over time.

Calculating the steady state velocity and zooming in to the altitude range that the ISR can see produces Figure 5.7. Up to 600 km there is good agreement between the calculated velocity and the modeled velocity. Above this region the calculated steady state velocity is grossly over or underestimated. The calculated velocity is positive when the ions are accelerating and negative when the ion are decelerating. This steady state velocity overestimation trend has been seen in both type 1 and type 2 simulations as well as the radar data.
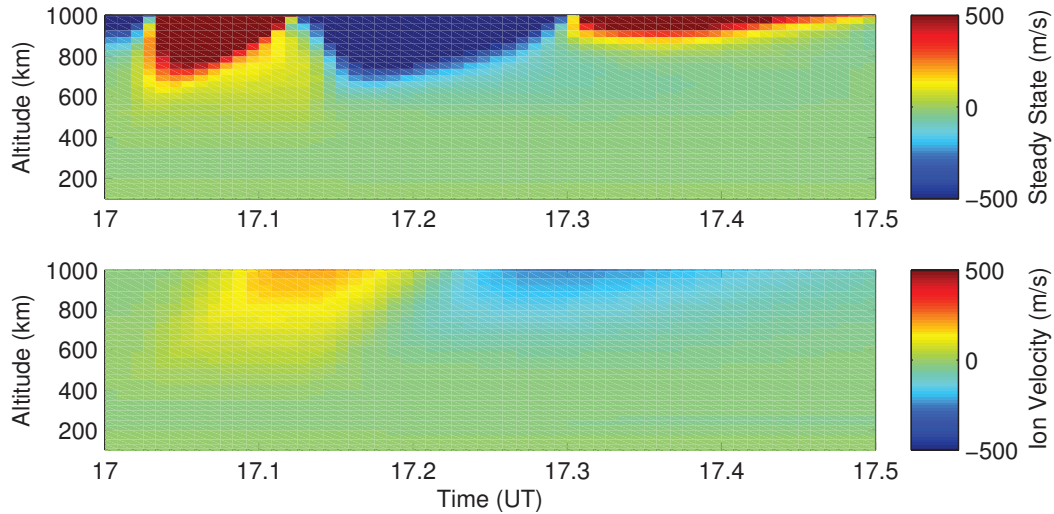
Figure 5.7: The calculated steady state velocity from the type 2 upflow modeled event.

5.2.3   Modeled Neutral Wind

Several upflow observations in the radar data have been attributed to the influence of neutral winds. In an effort to produce similarly structured upflows neutral wind simulations were created in GEMINI. Low altitude neutral winds, like those seen in the radar, are applied using a hyperbolic tangent description for the structure of the winds. Applying these for a duration of 7.5 minutes created the data in Figure 5.8. The neutral winds act on the ions by "dragging them along for the ride", thus the upflowing neutrals create the upflowing ions in panel 4. The decreasing electron temperature (panel 3) over time is due to the large electron densities that cause the electrons to cool rapidly even when the sun is up and is not due to the influence of neutral winds. The same is true for the ion temperatures (panel 2). The neutral wind driven upflow does not coincide with, or create, any heating in the ions or electrons. The low altitude, 200-400 km, initial increase in ion velocity (panel 4) corresponds

Figure 5.8: A modeled neutral wind driven upflow event.

to the location of the upflowing "pods" in the suspected neutral wind radar data. The strength of the applied neutral wind matches with suspected neutral winds seen in the radar data (50-75 m/s) and the propagation speed is describable by the wave propagation equations from Chapter 1.
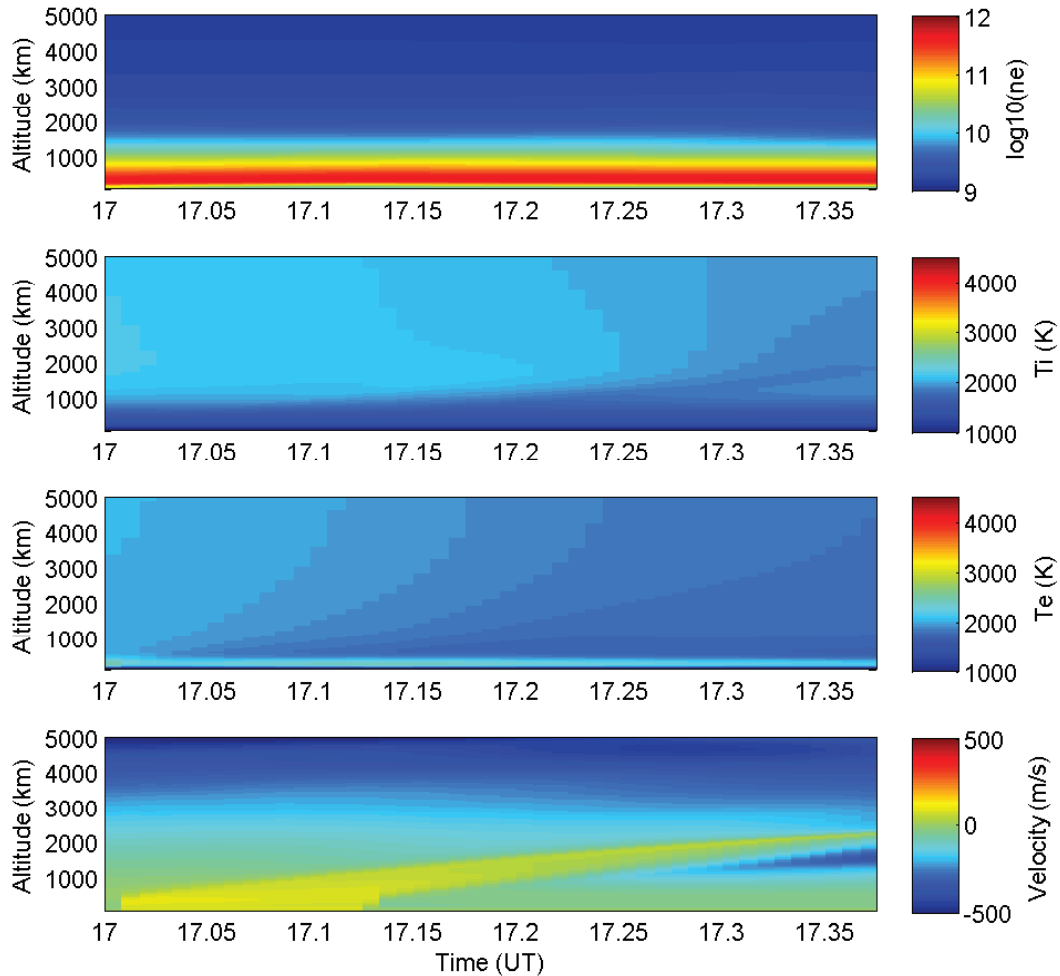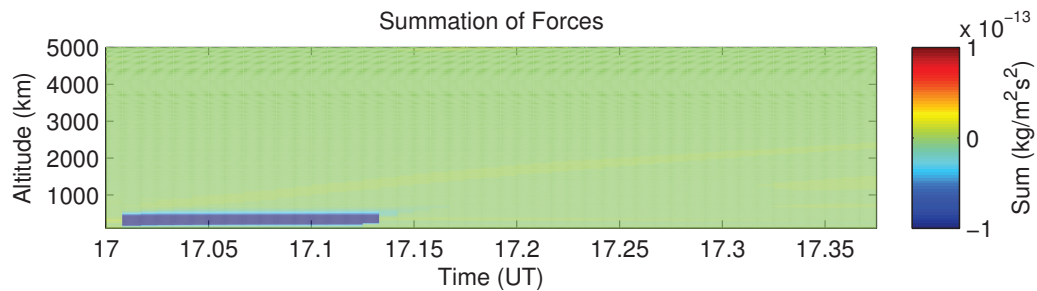
Figure 5.9: The sum of the forces from the neutral wind driven upflow event. The application of the neutral wind creates a strong, negative force because in the initial derivation of the force balance equation neutral wind effects were assumed to be zero.

Using the force balance equation the sum of the forces is calculated and presented in Figure 5.9. This sum for most of the simulation is balanced. There is a small amount of positive force in the temporal and spatial location of the upflowing ions. The initiation of the neutral wind has left a low altitude section, during the first 7.5 minutes of the simulation, imbalanced and highly negative. This is due to the original force balance calculation in which the neutral wind was assumed to be zero thus initiating neutral winds creates unaccounted for forces.

5.2.4 Modeled Dual Source Upflow

In the previous radar data Chapter, neutral winds have been inferred alongside other ion upflow processes. In order to determine how much neutral winds assist upflowing ions initiated by other processes a dual source upflow event was simulated that combines both a type 1 with an applied electric potential of 50 mV/m and the neutral wind discussed in Section 5.2.3. The electron density, ion temperature, electron temperature and O^+ velocity from this dual source upflow event are presented in Figure 5.10. The ion temperature (panel 2) at low altitudes, exhibits high tem-
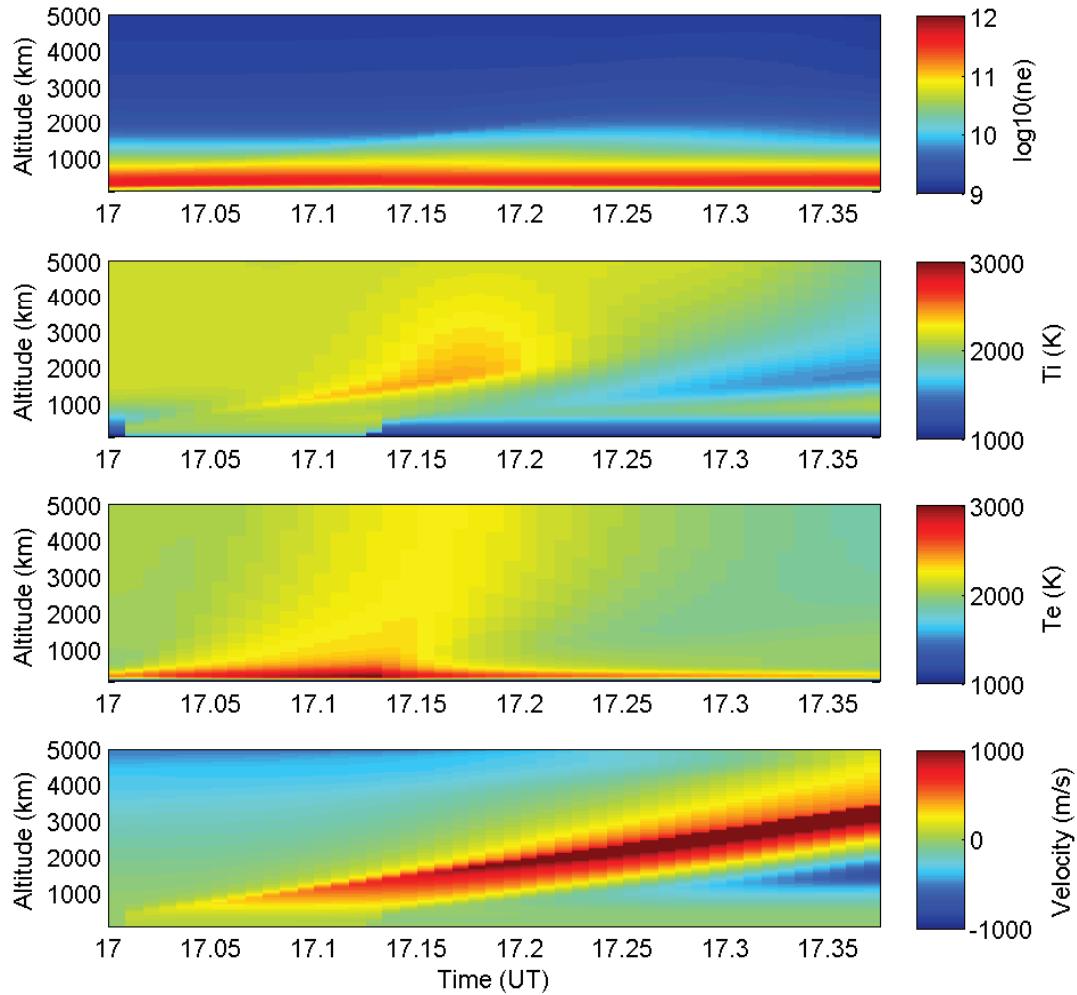
Figure 5.10: A dual source upflow event with type 1 and neutral wind driven upflow.

peratures up to 2000k from the applied electric potential. This causes the electron temperature (panel 3) to increase as well from the heat transfer between the ions and electrons. The electron density (panel 1) is lofted as the ionosphere is heated and upflowing. The ion upward velocity increases as the disturbance propagates through

altitude and time. The overall propagation speed is larger in this dual source upflow

than individually in either the type1 or neutral wind driven upflow, as expected.
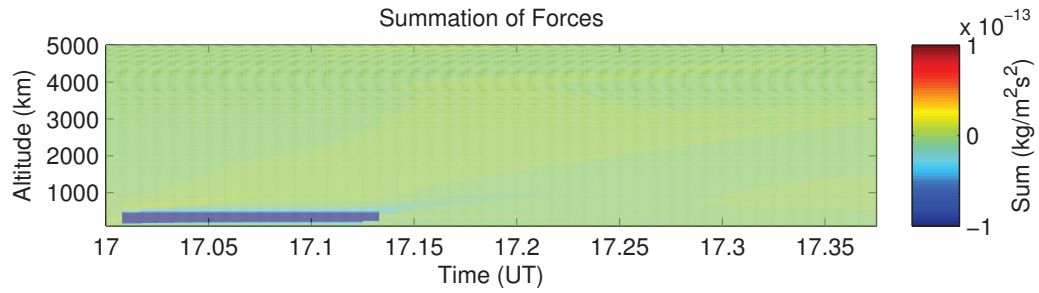
Figure 5.11: The sum of the forces for a dual source upflow event that is a combination of a type 1 and neutral wind driven upflow.
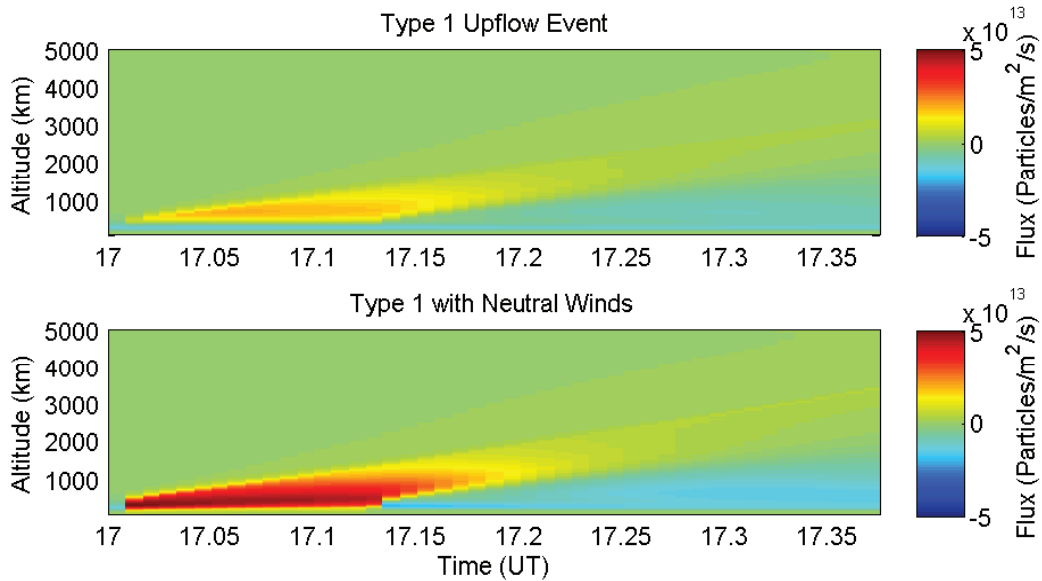
Figure 5.12: The flux in particles/m^2/s created by a type 1 upflow with an applied electric potential of 50 mV/m (panel 1) and that same type 1 upflow with neutral winds (panel 2).

Using the force balance analysis, the sum of the forces is presented in Figure 5.11. For most of the simulation the forces are balanced. There is a small amount of positive

net force in the temporal and spatial location of the upflowing ions. The initiation of the neutral wind has once again left a low altitude section highly negative. This is a result of the original force balance calculation not accounting for neutral winds.

The flux of particles created by the dual source upflow event (panel 2) and the type 1 event without the addition of any neutral wind (panel 1) are presented in Figure 5.12. The speed of the upflow as well as the corresponding flux are both larger in the dual source upflow. The presence of neutral winds in conjunction with upflows from other sources create stronger fluxes of ions.

5.2.5   Modeled Cavitation Upflows

Another cause of ion upflow is transverse energization, as mentioned in Chapter 1. At higher altitudes, transverse energization creates a depletion in the local density which affects ionospheric drift velocities. The exact spatial distribution of a density cavity created by this physical process is unknown so a Gaussian distribution has been selected to illustrate possible effects and features. Suddenly imposing a density cavity, as initial conditions, instead of creating it during the simulation is not detrimental to
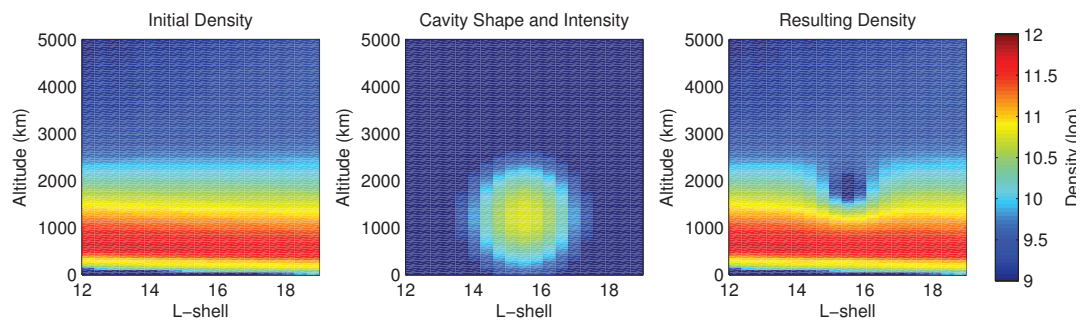
Figure 5.13: The before [left] and after [right] density profile in the cavity [center] creation process.

this preliminary look into possible response features. In Figure 5.13 the initial density distribution (panel 1) has the cavity at 50% depletion (panel 2) subtracted from it producing the density initial conditions (panel 3) used in the simulation. After the simulation, the center field line is selected for further analysis.
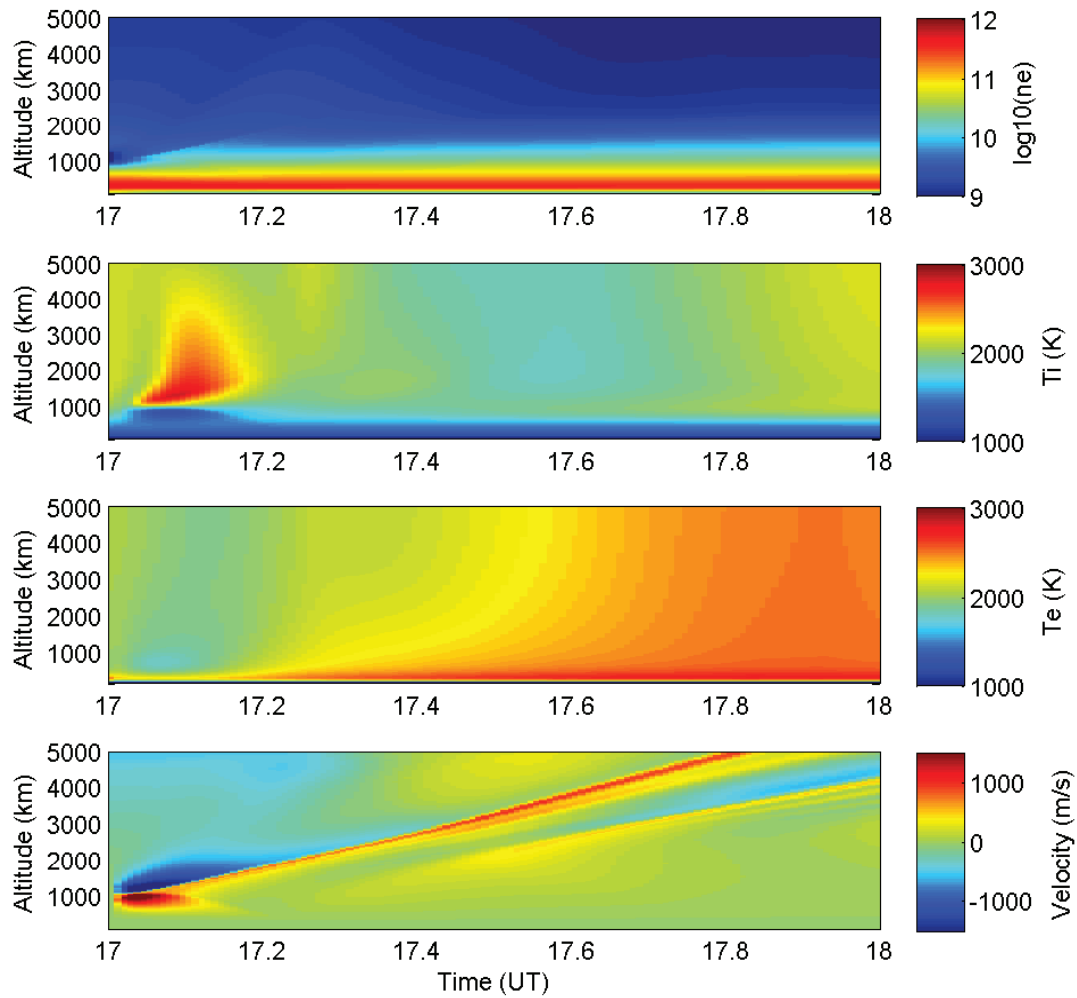
Figure 5.14: The modeled response to a density cavity at 50% reduction of the local ion populations.

Using the aforementioned density initial conditions, GEMINI was run for a total of 60 simulation minutes and produced the data in Figure 5.14. As expected, the density cavity acts as a vacuum and immediately starts to fill when the simulation starts. This creates large ion velocities above and below the cavity (panel 4). There is a corresponding change in the ion temperature (panel 2) from the expansion/compression effects and change in local densities. The electron temperatures (panel 3) at 17.2 UT are 1800 K initially but over time heat up to 2600 K as the higher altitude densities (panel 1) are decreased by the vacuum effects of filling the cavity and the resulting upflowing ions. The region of maximum velocity propagates upward almost twice as slow in this cavitational simulation than in the type 1 or type 2 simulations. ISR observable signatures of this phenomenon would include cooling in both electron and ion temperatures as well as ion upflow at high observable altitudes. While no signatures of this sort were found within the examined data it is likely that cavitationally driven upflows occur outside the observable range of ISR.

5.3 Parameter Summaries

To expand the investigation of these various upflow processes, a systematic study was conducted. The model was run for a wide range of inputs and upflow types in order to explore the sensitivity of ionospheric upflow to these energy inputs. The following state space plots of type 1, type 2 and cavitational upflows have been created to further compare and contrast the different features and responses of the events. For the type 1 modeled events the applied electric potential ranges from 50 to 150 mV/m in 10 mV/m increments. The type 2 modeled events have the electron precipitation effects peaking at a range from 2 to 20 mW/m^2 in 2 mW/m^2 increments. The cavity models

range from 10% depletion up to 80% depletion in 10% increments.The velocities at
500 km, across all of the aforementioned models, are plotted in Figure 5.15.

This altitude is still within the range of ISR allowing for a comparison between
observed and modeled velocities giving a rough estimate of upflow source strengths.

Figure 5.15: The velocity at 500 km across many simulations of type 1 [left], type 2 [center], and density cavities [right].

Figure 5.16: The ion flux at 500 km across the multitude of simulations of various types and strengths. Type 1 [left], type 2 [center], and density cavities [left] have been each modeled at various intensities.

The stronger energy sources create larger upflows, as expected, with the strongest type 1 events reaching velocities greater than 200 m/s. The cavitational upflows are not as rapidly upflowing at this altitude but the upflowing ions occur longer and maintain a minimum throughout the simulation of up to 50 m/s for the larger cavity

Figure 5.17: The velocity at 1000 km across many simulations of type 1 [left], type 2 [center], and density cavities [right].

Figure 5.18: The ion flux at 1000 km across the multitude of simulations of various types and strengths. Type 1 [left], type 2 [center], and density cavities [left] have been each modeled at various intensities for half an hour.

models. The ion flux at 500 km for all of the models is given in Figure 5.16. The locations of large flux match the locations of large upflows as expected.

Taking additional altitude slices at 1000 km, 2000 km and 3000 km, Figures 5.17, 5.19 and 5.21 are produced. The corresponding particle fluxes from the type 1,
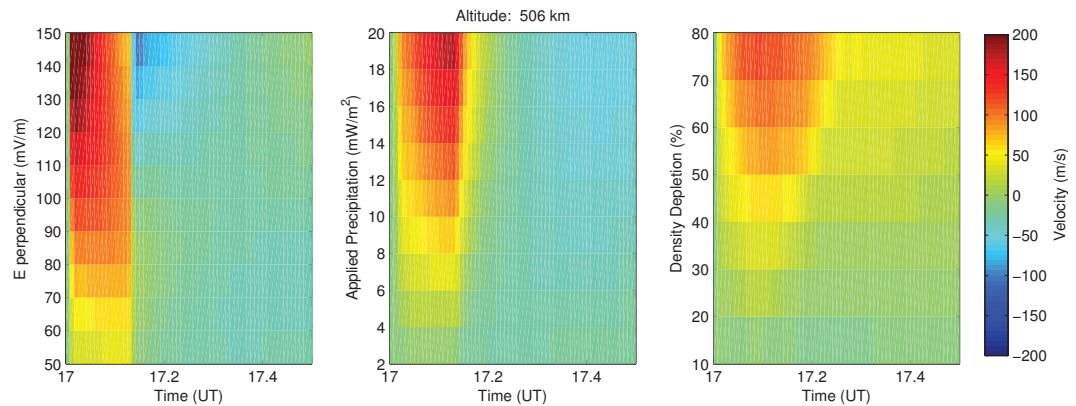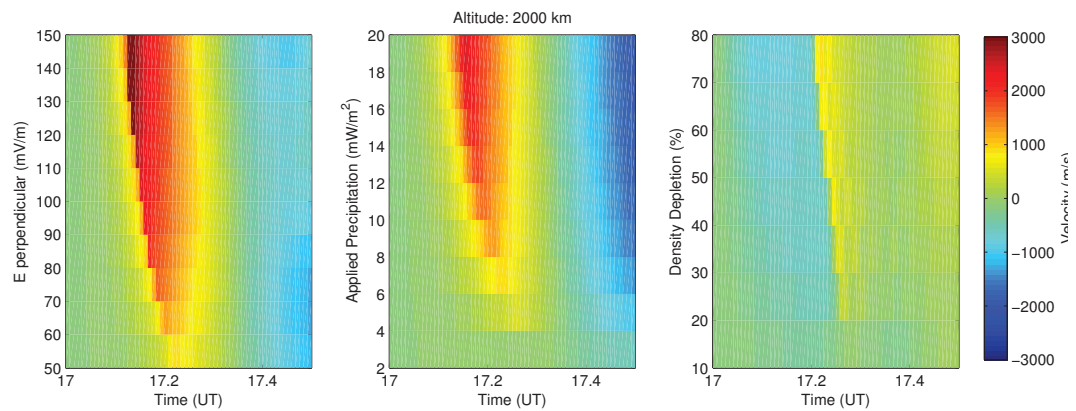

Figure 5.19: The velocity at 2000 km across many simulations of type 1 [left], type 2 [center], and density cavities [right].
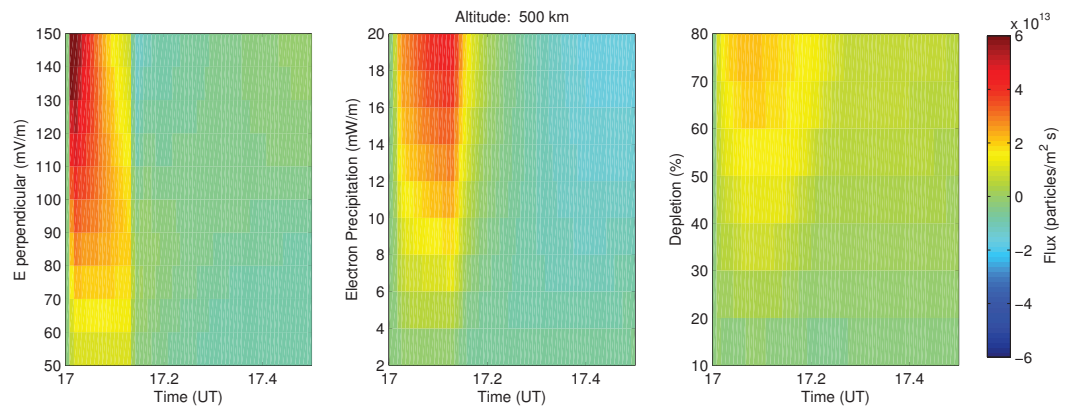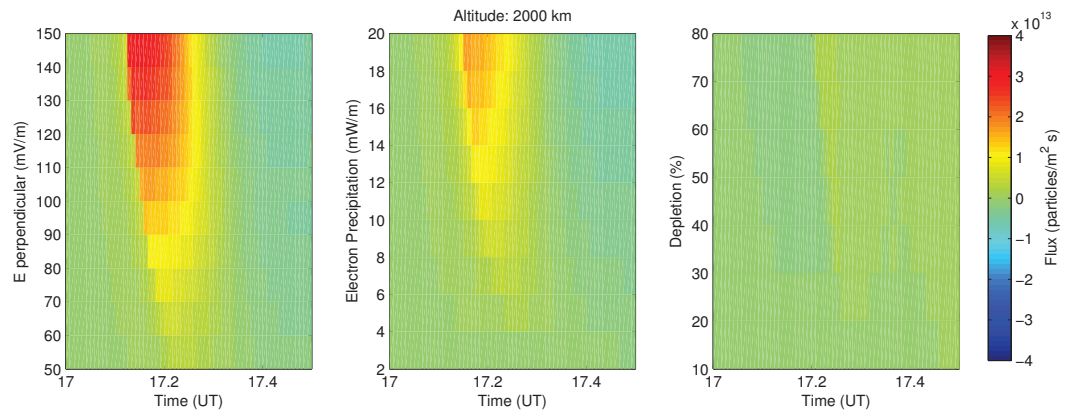

Figure 5.20: The ion flux at 2000 km across the multitude of simulations of various types and strengths. Type 1 [left], type 2 [center], and density cavities [left] have been each modeled at various intensities for half an hour.

type 2 and cavitational simulations are shown in Figures 5.18, 5.20, and 5.22. The peak velocity occurs at later and later times for higher and higher altitudes for all upflow strengths and types. This clearly illustrates the time dependent nature of ion upflows. Also, the faster the upflow is moving the sooner the peak velocity reaches
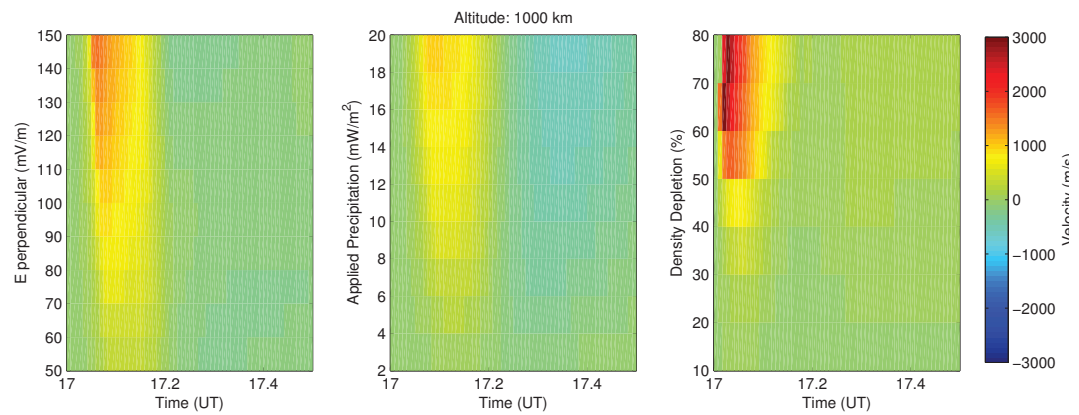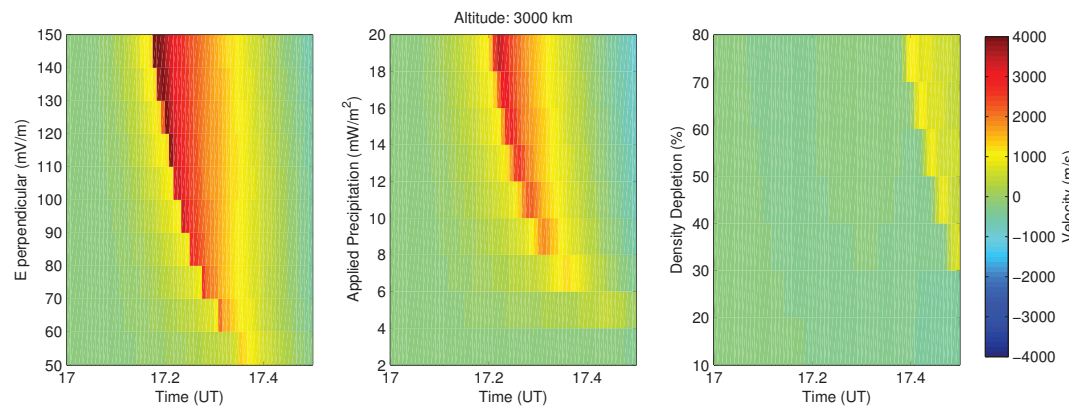

Figure 5.21: The velocity at 3000 km across many simulations of type 1 [left], type 2 [center], and density cavities [right].
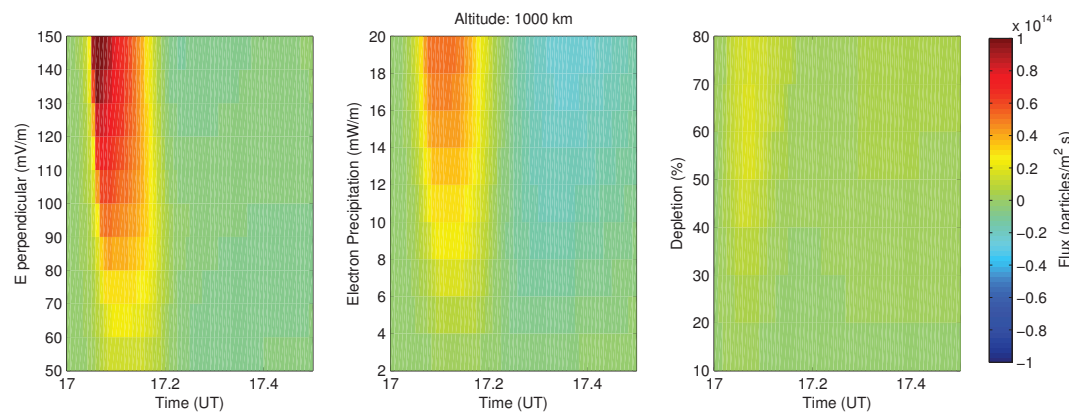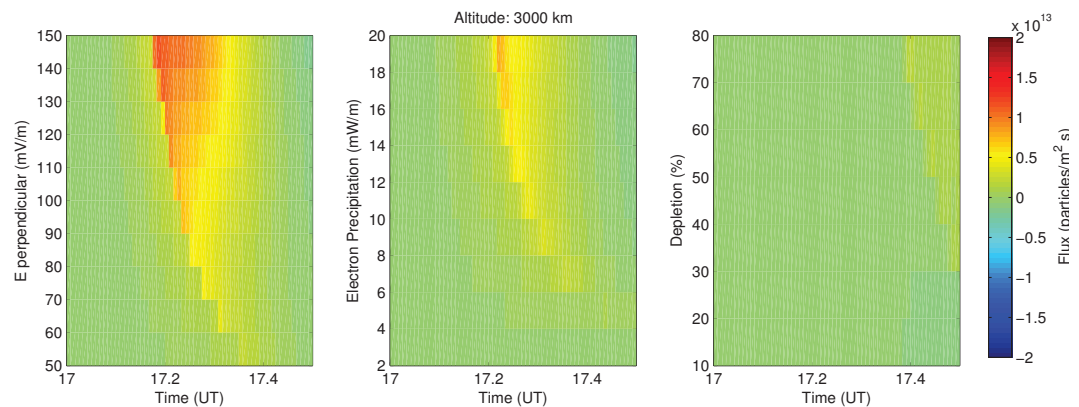

Figure 5.22: The ion flux at 3000 km across the multitude of simulations of various types and strengths. Type 1 [left], type 2 [center], and density cavities [left] have been each modeled at various intensities for half an hour.

an altitude. The time-delay and intensity of the source result in strong perturbations traveling faster in all cases and is the cause of the curve that develops in the higher altitude velocity and hence flux plots. On average, there are greater positive fluxes during times of upflow than the negative fluxes that occur during later on downflows.

Chapter 6

CONCLUSIONS

6.1 Radar and Modeling Conclusions

6.1.1 Distribution of Upflows

Observations of upflow events occur most often in the cusp and midnight auroral zone locations. Defining upflow types from radar data and creating simulations of them generates distinctions that are artificial and limiting because it is not as common to have singular heating of only the ions or only the electrons as it is to have both heated. Most of the observed upflows, 56%, had evidence of both ion and electron heating. While only a few events, 3%, had no clear heating sources. The other 41% of the observed upflow events had primarily elevated ions or electrons.

6.1.2 Limits of the Simplified Descriptions

Many methods of analysis may be limited to altitude regions or specific situations but they are still useful for inferring information about dynamic systems. At high

altitudes, and over large domains, ionospheric responses are not well characterized by the localized assumptions used here. The force balance calculation takes into consideration only four forces (Forces per unit volume) acting locally on the ionosphere. This includes the pressure gradient, gravitational effects, inertia and collisional forces and does not include the complications of heat flux, nonlinearity and transient effects. As a result, the simplified force balance equation is applicable best at lower altitudes where collisions dominate and a steady state is maintained within the ionosphere. High altitude responses are not pure, wavelike propagations and include the dissipative effects of heat fluxes and heat exchange. Together, these effects yield a complex behavior for the upflows. The calculated steady state velocity, for altitudes greater than 450 km, tends to grossly over or underestimate the ion velocity as seen in both the radar data and the simulations. From the model, when the ions are accelerating the steady state velocity is overestimated; where the ions are decelerating the steady state velocity is underestimated. This limits the ability, using this calculation, to capture and reproduce all upflows because some are initiated in the region that is inappropriately described by the steady state calculation. Additionally, the breakdown of the steady state description of the ionosphere at higher altitudes leads to a limitation in the empirical scaling laws. There were no instantaneous input/output relationships across all altitudes. In all cases a time dependence was observed. Ultimately, a fully time-dependent, nonlinear ionospheric model is necessary for any realistic attempt to model these upflows.

6.1.3 Modeling Time-Dependant Ion Upflows

From the systematic study, the state space plots in Figures 5.17, 5.19, and 5.21 illustrate a propagation time delay, between the F-region where the upflows are initiated and higher-altitudes, that is highly amplitude dependent. Steepening of the leading edge of large amplitude perturbations is also noted. Electric fields exceeding 110 mV/m^2 or particle fluxes exceeding 18 mW/m^2 create tremendous fluxes ($\sim 10^{13}$ m^{-3} s^{-1}) of plasma that likely act as source populations for other energization processes above the ionosphere. Above 750 km, high altitude responses are not purely wave-like and include the dissipative effects of heat fluxes and heat exchange along with other complexities such as the O$^+$ - H resonant charge exchange. From the cavitational simulations, cooling was seen in the topside in conjunction with the ion upflows. A reciprocal observation in the radar data was not found suggesting that this type of upflow is rare, may occur most often outside of the range of Sondrestrom's ISR, or perhaps not at all.

6.1.4 Neutral Wind Influences

Neutral winds, of various possible sources, appear to play a role in the observed upflows for many of the data sets examined in detail. This suggests that neutral winds are necessary to balance the forces in the lower altitude, steady state region for all of the radar data sets. Simulations show that neutral winds will directly affect upflowing ion velocities, strengthening them, and can enhance, by a factor of $\sim 2-4$, upward ion fluxes in the topside ionosphere.

6.2   Future Work

All of the simulations of ion upflows were completed using a daytime ionosphere. The responses of night time ionosphere may be different given the lack of solar photoionization and other temporal effects. Conducting a comparison between the day and night velocities and flux would give more information about how the features of ion upflows change with regard to time of day.

Working with high altitudes, several question have arisen. At what altitude does transverse energization become important? What role do electrodynamic effects play? And how appropriate are the system of moment equations and electrostatics used within this study for high altitudes? Answering these questions will give better insight into the bigger picture of ionospheric dynamics.

Bibliography

Andre, M., Norqvist, P., Andersson, L., Eliasson, L., Eriksson, A., Blomberg, L., Erlandson, R., and Waldemark, J. (1998). Ion energization mechanisms at 1700 km in the auroral region. *J. Geophys. Res.*, 103:4199–4222.

Bates, H. (1973). Atmospheric expansion through joule heating by horizontal electric fields. *Planet. Space Sci.*, 21(2073).

Benson, R., Calvert, W., and Klumpar, D. (1980). Simultaneous wave and particle observations in the auroral kilometric source region. *Geophys. Res. Lett.*, 7(959).

Block, L. and Falthammar, C. (1968). Effects of field-aligned currents on the structure of the ionosphere. *J. Geophys. Res.*, 73(4807).

Calvert, W. (1981). The auroral plasma cavity. *Geophys. Res. Lett.*, 8(919).

Diloy, P., Robineau, A., Linensten, J., Blley, P., and Fontanari, J. (1996). A numerical model of the ionosphere, including the e-region above eiscat. *Ann. Geophys.*, 14:191–200.

Endo, M., Fujii, R., Buchert, S. C., Nozawa, S., Watanabe, S., and Yoshida, N. (1999). Ion upflow and downflow at the topside ionosphere observed by the EISCAT vhf radar. *Ann. Geophys.*, 18:170–181.

Foster, C. and Lester, M. (1996). Observations of nightside auroral plasma upflows in the f-region and topside ionosphere. *Ann. Geophys.*, 14:1274.

Foster, C., Lester, M., and Davies, J. A. (1998). A statistical study of diurnal, seasonal and solar cycle variations of f-region and topside auroral upflows observed by eiscat between 1984 and 1996. *Ann. Geophys.*, 16:1144–1158.

Ganguli, S. B., Palmadesso, P. J., and Mitchell, H. G. (1988). Effects of electron heating on the current driven electrostatic ion cyclotron instability and plasma transport processes along auroral field lines. *Geophys. Res. Lett.*, 15(11):1291–1294.

Gurnett, D. and Bhattacharjee, A. (2005). *Introduction to Plasma Physics.* Cambridge University Press, Cambridge.

Hunsucker, R. (1982). Atmospheric gravity waves generated in the high-latitude ionosphere: A review. *Reviews of Geophysics*, 20.

Jones, G., Williams, P., and Winser, K. (1990). Large ionospheric plasma flows along magnetic field lines: Esciat observations and interpretations. *Adv. Space Sci.*

Jones, G., Williams, P., Winser, K., Lockwood, M., and Suvanto, K. (1988). Large plasma velocities along the magnetic field line in the auroral zone. *Nature*, 336(231).

Keating, J. G., Mulligan, F. J., and Doyle, D. B. (1990). A statistical study of large field-aligned flows of thermal ions at high-latitudes. *Planet. Space Sci.*, 38(9):1187–1201.

Kelley, M. C. (2009). *The Earth's Ionosphere: Plasma Physics and Electrodynamics.* Academic Press.

King, J. and Kohl, H. (1965). Upper atmospheric winds and ionospheric drifts caused by neutral air pressure gradients. *Nature*, 206:699–701.

Kintner, P. M., Bonnell, J., Arnoldy, R., Lynch, K., Pollock, C., and Moore, T. (1996). SCIFER-Transverse ion acceleration and plasma waves. *Geophys. Res. Lett.*, 23:1873–1876.

Lynch, K. A., Semeter, J. L., Zettergren, M., and Kinter, P. (2007). Auroral ion outflow: Low altitude energization. *Ann. Geophys.*, 25.

Moen, J., Oksavik, K., and Carlson, H. C. (2004). On the relationship between ion upflow events and cusp auroral transients. *Geophys. Res. Lett.*, 31:11808.

Moore, T. E. and Horwitz, J. L. (2007). Stellar ablation of planetary atmospheres. *J. Geophys. Res.*, 45:1944–9208.

Ogawa, Y., Buchert, S. C., Fujii, R., Nozawa, S., and van Eyken, A. P. (2009). Characteristics of ion upflow and downflow observed with european incoherent scatter svalbard radar. *J. Geophys. Res.*, 114.

Ogawa, Y., Buchert, S. C., Sakurai, A., Nozawa, S., and Fujii, R. (2010). Solar activity dependence of ion upflow in the polar ionosphere observed with the european incoherent scatter (eiscat) tromsÃ¸ uhf radar. *Journal of Geophysical Research.Space Physics*, 115(7).

Ogawa, Y., Fujii, R., Buchert, S. C., Nozawa, S., and Ohtani, S. (2003). Simultaneous eiscat svalbard radar and dmsp observations of ion upflow in the dayside polar ionosphere. *J. Geophys. Res.*, 108:1101.

Ogawa, Y., Seki, K., Hirahara, M., Asamura, K., Sakanoi, T., Buchert, S., Ebihara, Y., Obuchi, Y., Yamazaki, A., Sandahl, I., Nozawa, S., and Fujii, R. (2008). Coordinated eiscat svalbard radar and reimei satellite observations of ion upflows and suprathermal ions. *J. Geophys. Res.*, 113(A5).

Picone, J. M., Hedin, A. E., Drob, D. P., and Aikin, A. C. (2002). Nrlmsise-00 empirical model of the atmosphere: Statistical comparisons and scientific issues. *Journal of Geophysical Research: Space Physics*, 107(A12):2156–2202.

Remick, K. J. (2004). A statistical characterization of the high latitude ionosphere with a focus on possible source mechanisms for ion upwelling. Master's thesis, University of Alaska Fairbanks.

Rishbeth, H. and Garriott, O. (1969). *Introduction to ionospheric Physcis*. Academic Press.

Schunk, R. W. (1977). Mathematical structure of transport equations for multispecies flows. *Reviews of Geophysics*, 15(4):429–445.

Schunk, R. W. and Nagy, A. (2000). *Ionospheres*. Cambridge University Press, Cambridge.

Semeter, J., Heinselman, C. J., Thayer, J. P., Doe, R. A., and Frey, H. U. (2003). Ion upflow enhanced by drifting F-region plasma structure along the nightside polar cap boundary. *Geophys. Res. Lett.*, 30:2139.

Sheffield, J., Froula, D., Glenzer, S., and Luhmann, N. (2011). *Plasma Scattering of Electromagnetic Radiation (Second Edition)*. Academic Press, Boston, second edition edition.

Singh, N. (1992). Plasma perturbations created by transverse ion heating events in the magnetosphere. *Journal of Geophysical Research: Space Physics*, 97(A4):4235–4249.

Singh, N., S. Hwang, D. T., and Richards, P. (1989). Temporal features of the outflow of heavy ionospheric ions in response to a high altitude plasma cavity. *Geophys. Res. Lett.*, 16(29).

Skjaeveland, A., Moen, J., and Carlson, H. C. (2011). On the relationship between flux transfer events, temperature enhancements, and ion upflow events in the cusp ionosphere. *Journal of Geophysical Research: Space Physics*, 116(A10).

Solomon, S. and Qian, L. (2005). Solar extreme-ultraviolet irradiance for general circulation models. *J. Geophys. Res.*, 110.

St. Maurice, J. P. and Laneville, P. J. (1998). Reaction rate of O^+ with O_2, N_2, and *NO* under highly disturbed auroral conditions. *Geophys. Res. Lett.*, 103.

Strangeway, R. J., Ergun, R. E., Su, Y. J., Carlson, C. W., and Elphic, R. C. (2005). Factors controlling ionospheric outflows as observed at intermediate altitudes. *J. Geophys. Res.*, 110.

Su, Y. Z. (1999). Altitude dependencies in the solar activity variation of the ionospheric electron density. *J. Geophys. Res.*, 104:14879–14891.

Wahlund, J.-E., Opgenoorth, H. J., Häggström, I., Winser, K. J., and Jones, G. O. L. (1992). EISCAT observations of topside ionospheric ion outflows during auroral activity: Revisited. *J. Geophys. Res.*, 97(A3):3019–3037.

Whitteker, J. (1977). The transient response of the topside ionosphere to precipitation. *Planet. Space Sci.*, 25(773).

Yoshida, N., Watanabe, S., Fukunishi, H., Sakanoi, T., Mukai, T., Hayakawa, H., Matsuoka, A., Kasahara, Y., Fujii, R., Nozawa, S., and Ogawa, Y. (1999). Coordinated akebono and EISCAT observations of suprathermal ion outflow in the nightside inverted-v region. *J. Atmos. Sol. Terr. Phys.*, 62:449–465.

Zettergren, M. and Semeter, J. (2012). Ionospheric plasma transport and loss in auroral downward current regions. *J. Geophys. Res.*, 117.

Zettergren, M., Semeter, J., Blelly, P. L., and Diaz, M. (2007). Optical estimation of auroral ion upflow: Theory. *J. Geophys. Res.*, 112.

Zettergren, M., Semeter, J., Heinselman, C., and Diaz, M. (2011). Incoherent scatter radar estimation of f-region ionospheric composition during frictional heating events. *J. Geophys. Res.*, 116.